Research Square

Preprints are preliminary reports that have not undergone peer review.
They should not be considered conclusive, used to inform clinical practice,
or referenced by the media as validated information.

Structural insight into dual roles of MeCP2 in chromatin architecture regulation

Tengfei Lian

liantengfei@cpu.edu.cn

China Pharmaceutical University

Ruifang Guan

Nanjing university

Rui Ren

China Pharmaceutical University

Weiwei Ji

Nanjing Agriculture University

Yanhua Wang

China Pharmaceutical University

Qilong Yao

School of Life Science, Nanjing university

Article

Keywords:

Posted Date: November 13th, 2026

DOI: https://doi.org/10.21203/rs.3.rs-10396144/v1

License: This work is licensed under a Creative Commons Attribution 4.0 International License.
Read Full License

Additional Declarations:

There is **NO** Competing Interest.

All the cryo-EM maps and model files presented in the paper were uploaded to Figshare (https://figshare.com)

Structural insight into dual roles of MeCP2 in chromatin architecture regulation

Rui Ren[1], Weiwei Ji[1], Yanhua Wang[1], Qilong Yao[2], Ruifang Guan[2,*], Tengfei Lian[1,*]

[1]Jiangsu Provincial Key Laboratory of Biology and Therapeutics for Immune System-Related Diseases, School of Life Science and Technology, China Pharmaceutical University, Nanjing, China.

[2]School of Life Science, Nanjing University, Nanjing, China.

[*]Correspondence: Tengfei Lian (e-mail: liantengfei@cpu.edu.cn), Ruifang Guan (ruifang.guan@nju.edu.cn).

Abstract

Rett syndrome protein MeCP2 binds broadly to both free DNA and nucleosomes, modulating chromatin architecture and either repressing or activating gene expression. However, the mechanisms by which MeCP2 engages with nucleosomes and alters chromatin structure remain elusive. Here, we present cryo-electron microscopy structures of MeCP2-bound nucleosomes reconstituted on W601 DNA and α-satellite DNA, as models for inaccessible and accessible chromatin, respectively. We find that MeCP2 molecules bind at nucleosome SHL ± 6.5 regardless of DNA sequences through interacting with DNA gyres, immobilizing linker DNA to facilitate nucleosome condensation in W601 nucleosome. In contrast, in α-satellite nucleosome, additional MeCP2 molecules localize to SHL ± 1.5 via contacts with both DNA and H3, evicting MeCP2 at SHL ± 6.5 and leading to nucleosome unwrapping. Collectively, our findings reveal that MeCP2 exhibits distinct binding behaviors on nucleosomes compared to naked DNA, and uncover its dual-mode molecular mechanism for regulating chromatin architecture and accessibility.

Main

Rett syndrome (RTT) is a severe postnatal neurodevelopmental disorder, characterized by intellectual and motor disabilities that manifest after 6-18 months of normal development. RTT is caused by the mutations in an X-linked gene *methyl-CpG-binding protein 2* (*MECP2*)[1-4]. Gene duplication of *MeCP2* leads to MeCP2 duplication syndrome, which is also severely detrimental to the nervous system. MeCP2 was initially identified as a reader of methylated CpG (mCG) sites across the genome[5-7]. Subsequent studies revealed that it also binds non-CpG methylated sites such as mCAC and unmethylated sequences such as CA repeats[8-15]. Moreover, MeCP2 is a major reader of 5-hydroxymethylcytosine (5hmC)[16,17]. The broad DNA-binding versatility underpins its multifaceted roles in gene regulation, as MeCP2 primarily induces gene repression through diverse mechanisms while also activating a subset of genes[10,18-22].

MeCP2 consists of five domains (Fig. 1a). The DNA-binding specificity is primarily attributed to the methyl-CpG-binding domain (MBD) of MeCP2[23], the only structured domain conserved among all methyl-CpG binding proteins. Other domains also exhibit DNA-binding ability, although their functions remain largely unclear[24,25]. In addition, the transcriptional repression domain (TRD) interacts with SIN3A histone deacetylase (HDAC) complex, and the NCoR-SMRT interaction domain (NID) recruits NCoR/SMRT corepressor complexes, both leading to transcriptional inhibition[5,26]. Notably, MeCP2-induced gene repression persists in the absence of TRD and NID, indicating the existence of additional repression mechanisms[27-30]. The intervening domain (ID) is an additional DNA-binding domain implicated in heterochromatin compaction and RTT, although its precise function remains unknown[25,31-33].

In vitro biochemical and single-molecule imaging studies demonstrated that MeCP2 tightly bound and stabilized nucleosomes[24,28,34], and ChIP-seq combined with MNase-seq confirmed prominent co-localization of MeCP2 and nucleosomes in cells[35]. Moreover, MeCP2 has been regarded as a linker histone-like protein that compacts nucleosomes into higher-order heterochromatin structures, similar to linker histone H1[36-39]. The association with nucleosomes and heterochromatin is critical for gene regulation and proper neuronal development. Conversely, MeCP2 could localize to microsatellite sequences to maintain nucleosome-free regions[16], suggesting its divergent effects on chromatin architecture. Collectively, the lack of mechanistic insights into MeCP2-mediated chromatin structure alterations hinders our understanding of its complex effects on chromatin accessibility and gene transcription.

Here, we determined the cryo-electron microscopy (cryo-EM) structures of MeCP2 bound to nucleosomes containing W601 and α-satellite DNA, which form inaccessible and accessible chromatin, respectively. Our findings illustrate that MeCP2 molecules bind at entry/exit sites in W601 nucleosomes to rigidify linker DNA, stabilizing nucleosome and preserving higher-order chromatin structure. In contrast, MeCP2 bound at superhelical location (SHL) ± 1.5 displaces the entry/exit-site MeCP2 molecules, ultimately causing nucleosome unwrapping in α-satellite nucleosome. Together, our findings provide a mechanistic basis for understanding the broad spectrum of MeCP2-mediated chromatin organization.

Results

Relationship between chromatin accessibility and GC content

Previous ChIP-seq data suggested that preference for mCG sites, which correlated with heterochromatin, is partially attributed to the enrichment of MeCP2 at high GC content (GC%) regions[40,41]. Motivated by this observation, we analyzed MeCP2 binding sites on nucleosome and characterized the relationship between chromatin accessibility and local GC% by plotting the distribution of ATAC-seq signal (Fig. 1b). The majority of MeCP2-associated nucleosomes, identified by overlapping ChIP-seq and MNase-seq peaks, localized to regions of low ATAC-seq signal, particularly for high GC% sequences. In contrast, a minority of peaks with high ATAC-seq signal mostly contained low GC% sequences (GC% < 50%) (Fig. 1b). This result implied that GC% was related to chromatin accessibility at MeCP2-associated nucleosome sites. To investigate the underlying mechanism, we reconstituted nucleosome with 177 bp α-satellite DNA with low GC% (41.8%) as a representative of accessible chromatin, since MeCP2-bound α-satellite nucleosomes exhibited high ATAC-seq signals (Fig. 1c and Extended Data Fig. 1a). Moreover, we reconstituted nucleosome containing 187 bp W601 sequence with high GC% (57.8%) as a representative of inaccessible chromatin (Extended Data Fig. 1a), as earlier research showed that MeCP2 protected W601 nucleosome from MNase digestion and induced nucleosome compaction[28,34,36].

Structures of W601 nucleosome bound by MeCP2

Prior sequencing data implied that localization of MeCP2 to nucleosome was not dependent on DNA methylation, despite its preference for mCG[35]. Nevertheless, CpG methyltransferase treated W601 DNA was used for nucleosome preparation (Extended Data Fig. 1b). An scFv targeting H2A-H2B acidic patch was confirmed to co-bind nucleosome with MeCP2 by electrophoretic mobility shift assay (EMSA; Extended Data Fig. 1c), and was applied to improve the cryo-EM sample stability against air-water interface without crosslinking[42]. Structures of W601 nucleosome (termed nucleosome^{601}) bound by one or two MeCP2 molecules were determined at near atomic resolution of 3.0 Å and 2.8 Å, with additional density at entry/exit sites corresponding to MeCP2 (Fig. 1d,e and Extended Data Fig. 2 and 3, Table 1). Residues 92 to 162 in the MBD and part of the ID from residues 163 to 169 were modelled based on the MeCP2-DNA crystal structures, and extended density connecting ID was not able to be modelled due to the low local resolution.

The structures of MeCP2-bound nucleosome^{601} revealed that MBD domains bound at symmetric positions at SHL ± 6.5 on a fully wrapped nucleosome (Fig. 1d), distinct from H1 location at dyad[43]. In naked DNA, MeCP2 widens the major groove[7,16,44]. In the nucleosome^{601}, however, DNA major groove structures at SHL ± 6.5 remained unchanged upon MeCP2 binding, since H3 N-terminal tail laid in the minor groove on the opposite side prevented major groove widening (Extended Data Fig. 3c). Deeper 3D classification addressed extended ID density that laid along the DNA track and contacted DNA backbone (Fig. 1f and Extended Data Fig. 2c), supporting the notion that ID served as an additional DNA binding domain. EMSA using an ID truncated mutant (termed MeCP2$^{\Delta ID}$) showed lower affinity to nucleosome than wild type (WT) MeCP2, suggesting that ID directly contributed to MeCP2 binding to nucleosome (Fig. 1f and Extended Data Fig. 1d,e).

MeCP2 promotes unwrapping of α-satellite nucleosome

We next used the same scFv-assisted cryo-EM method to investigate the structure of unmethylated α-satellite nucleosome (termed nucleosome^{satellite}) bound by MeCP2 and identified multiple conformations (Fig. 2a-e and Extended Data Fig. 4 and 5, Table 1). Two MeCP2 molecules occupied the same SHL ± 6.5 sites as in the MeCP2-bound nucleosome^{601} structure, suggesting that SHL ± 6.5 were the universal MeCP2 locations on nucleosomes regardless of DNA sequences. However, densities of MeCP2 at SHL ± 6.5 were blurry and the loop between β1 and β2 (termed L2 loop) was disordered (Fig. 2b), due to the presence of two additional MeCP2 molecules at SHL ± 1.5 that inserted into the DNA gyres and destabilized MeCP2 molecules at SHL ± 6.5 through steric clash (Fig. 2c). Furthermore, 3D classification identified nucleosome classes with either one or both entry/exit sites unwrapped (Fig. 2d,e). The free nucleosome^{satellite} structure exhibited well-wrapped state (Fig. 2f and Extended Data Fig. 6, Table 1), indicating that insertion of MeCP2 into DNA gyres disrupted nucleosome structure and ultimately exposed nucleosomal DNA.

To verify the hypothesis, MNase digestion assay was performed on nucleosome^{601} and nucleosome^{satellite} (Fig. 2g). MNase-treated nucleosome^{601} without MeCP2 yielded a sharp band around ~147 bp, indicating removal of linker DNA with only nucleosomal core DNA kept. MeCP2 protected linker DNA in nucleosome^{601} as indicated by the longer DNA fragments after digestion of MeCP2-bound sample compared to the MeCP2-free sample. For nucleosome^{satellite}, MNase treatment generated smear bands with majority above ~147 bp. MeCP2 incorporation led to prominent cleavage deeper inside nucleosome^{satellite} core, as reflected by the shorter DNA fragment than ~147 bp in MeCP2-bound nucleosome^{satellite}. This result unveiled the opposite effects of MeCP2 on nucleosomes: protecting nucleosome^{601} while distorting nucleosome^{satellite}, consistent with our structures and the relationship between GC% and chromatin accessibility at MeCP2-associated nucleosomes (Fig. 1b,c). Together, the steric exclusion between multiple MeCP2 molecules represented a unique mechanism by which the same protein regulated chromatin accessibility in a DNA sequence dependent manner.

Interaction between MeCP2 and nucleosomal DNA

In crystal structures of MeCP2-DNA complexes, MeCP2 recognized canonical ‘CG’ and ‘CAC’ motifs through the hydrogen bonds between R111, R133 and DNA bases (Fig. 3a) [7,16,44]. Surprisingly, in nucleosomes, most MeCP2 molecules were positioned at previously unreported non-canonical sites rather than ‘CG’ or ‘CAC’ sites (Fig. 3b,c and Extended Data Fig. 3a,b and 5). In MeCP2-bound nucleosome^{601} structure, R111 and R133 interacted with ‘TTC’ and ‘CAT’ sites at SHL ± 6.5 (Fig. 3b). In MeCP2-bound nucleosome^{satellite} structure, ‘GA’ and ‘AT’ sites were recognized by MeCP2 at SHL ± 6.5, whereas ‘TC’ and ‘CAC’ sites were bound by MeCP2 at SHL ± 1.5 (Fig. 3c). Detailed interactions between MeCP2 and nucleosome^{satellite} DNA at SHL – 6.5 and SHL + 1.5 were not fully defined owing to the blurry EM densities, and corresponding motifs were determined by superposition of MeCP2-DNA crystal structures into the EM map. A fifth MeCP2 showed up at SHL – 5.5, contacting an ‘AT’ site. Despite the distinct motifs, MeCP2 interacted with nucleosomal DNA in a manner similar to that with naked DNA, demonstrating the plasticity of DNA recognition by MeCP2. The presence of four different recognition sites at analogous binding locations (SHL ± 6.5) and two distinct DNA sites at symmetric SHL ± 1.5 suggested that position played a key role in nucleosome targeting by MeCP2. Given that MeCP2 density was observed at SHL

± 1.5 in nucleosome^{satellite} but was absent at the equivalent position in nucleosome^{601}, we concluded that MeCP2 retained its DNA recognition specificity on nucleosomes.

MBD directly interacts with histone H3

Structural analysis showed that MeCP2 at SHL – 1.5 directly contacted histone H3 at two loci in nucleosome^{satellite} (Fig. 3d). MeCP2 R115 interacted with H3 E50 and Y54, and carbonyl oxygen of the G114 peptide bond formed electrostatic interaction with H3 R53. In addition, the density of H3 N-terminal tail flipped towards MeCP2 and fused with density of MBD, indicative of the interaction between MBD and H3 N-terminus. We carried out pull-down assay to examine the direct interaction (Fig. 3e), using untagged H3-H4 tetramers and MeCP2 with MBP-tag and his-tag. WT H3-H4 tetramer (termed H3^{WT}-H4) was pulled down by WT MeCP2. However, R115A mutant MeCP2 (termed MeCP2^{R115A}) exhibited reduced binding to H3^{WT}-H4, as reflected by weaker bands in the pull-down sample, and showed no interaction with H3$^{\Delta N}$-H4 (H3$^{\Delta N}$ denotes N-terminus truncated H3). The result demonstrated that MeCP2 interacted with H3 N-terminal tail and α1 helix, as observed in the EM density. Intriguingly, the R115 mutation has been identified in RTT patients[45], suggesting that its physiological function merits further examination.

MeCP2 immobilizes nucleosome^{601} linker DNA

MeCP2 underwent conformational change upon binding to nucleosome^{601} (Fig. 4a). Compared with the elongated shape of β1-L2-β2 in MeCP2-DNA complexes, the L2 loop became flattened to accommodate the DNA gyres in MeCP2-nucleosome^{601} complex. K112, S113 and R115 formed electrostatic interactions with the phosphate backbone of DNA from the opposing gyre (Fig. 4b), enabling MeCP2 to serve as a molecular glue to stabilize the dynamic entry/exit site DNA. To test the contribution of this interaction, we measured the apparent K_D of MeCP2-nucleosome binding and found that a triple mutant containing K112A, S113A, and R115A (termed MeCP2^{KSRmut}) exhibited lower affinity than WT MeCP2 (Fig. 4c and Extended Data Fig. 1d,f).

Although linker DNA and entry/exit site DNA are often poorly resolved in conventional nucleosome structures, the presence of MeCP2 markedly improved their visibility, owing to MeCP2-mediated bridging of DNA gyres (Fig. 1d,e). In the nucleosome^{601} harboring one MeCP2 structure, linker DNA density was observed only on the MeCP2 occupied side and was absent on the opposite side, implying that MeCP2 immobilized the nucleosomal linker DNA. Additionally, upon MeCP2 binding, disordered H2A C-terminal tail became visible and inserted into the major groove between DNA gyres adjacent to the H3 N-terminus (Fig. 4d). Basic H2A C-terminal tail making contact with DNA provided further restriction to the linker DNA, a feature also observed in H1-bound nucleosomes[43]. However, the linker DNA immobilized by H1 was more concentrated to the nucleosome core (Fig. 4e), discernable from that induced by MeCP2. Distinctive linker DNA conformation supported the finding that MeCP2 induced a heterochromatin state distinguishable from that promoted by H1[36].

To substantiate this hypothesis, we performed fluorescence resonance energy transfer (FRET) assay using 187 bp nucleosome^{601} with the two DNA termini labelled with Cy3 and Cy5, respectively (Fig. 4f). The FRET signal was low in free nucleosome but elevated enormously with H1 added, consistent with the ability of H1 to bring flexible linker DNA into close

proximity. Upon incorporation of MeCP2, the FRET signal also increased prominently, supporting the hypothesis that MeCP2 stabilized nucleosome^{601} linker DNA.

MeCP2 preserves heterochromatin architecture

Cell-based and biochemical assays demonstrated that MeCP2 was involved in heterochromatin condensation[36-39]. To investigate the mechanism of nucleosome compaction, we reconstituted nucleosome array (NA) encompassing unmethylated 4 × 197 bp W601 DNA, attempting to solve the structure of NA bound by MeCP2 (Extended Data Fig. 7). 2D class averages revealed stacked tetra-nucleosome and di-nucleosome classes (Fig. 5a and Extended Data Fig. 7d), however, 3D reconstruction yielded only a low resolution di-nucleosome map (Fig. 5b and Table 1). The di-nucleosome map contains two parallel nucleosomes with slightly tilted orientation, in which MeCP2 could be spatially placed between two nucleosomes without steric clash (Extended Data Fig. 8a). In addition, the conformation of the di-nucleosome map showed similar architecture to previously solved NA structures (Extended Data Fig. 8b,c)[46-48]. Focusing on mono-nucleosome using smaller box size during particle extraction generated well-defined mono-nucleosome map containing MeCP2 molecules at SHL ± 6.5 (Fig. 5c, left). MeCP2 positions in this structure were identical to that in methylated 187 bp mono-nucleosome^{601} bound by scFv and MeCP2 structure (Fig. 1d and Extended Data Fig. 7d-g), indicating that positions of MeCP2 on nucleosome^{601} were independent of overall DNA methylation status and scFv incorporation. In another 3D class, an extra density corresponding to MeCP2 was located at linker DNA and caused DNA bending around 35° (Fig. 5c, right). The observed variability in linker DNA angles indicated the potential structural heterogeneity of MeCP2-induced heterochromatin.

Previous studies identified three AT hook domains that were closely related to RTT[23,49]. We identified an additional fragment within ID upstream of AT hook 1, termed AT hook 0 in this work, showing considerable sequence similarity to other AT hook domains (Fig. 5d). Given the importance of ID, AT hook domains and L2 loop in DNA binding and potential heterochromatin compaction, we further investigated their contributions to NA maintenance using enzyme cleavage assay (Fig. 5e). Restricted endonuclease SmaI, whose cutting sites were located at linker DNA, was applied to digest 6 × 197 bp NA with MeCP2 and its mutants associated. Free NA was digested extensively, whereas NA bound by WT MeCP2 remained largely intact. Truncation of AT hook 0 (MeCP2$^{\Delta hk0}$) or AT hook 1 (MeCP2$^{\Delta hk1}$) alone led to a modest increase in digestion efficiency, while MeCP2$^{\Delta ID}$ and MeCP2^{KSRmut} caused a substantial increase. This result demonstrated that AT hook 0, AT hook 1 together with L2 loop were involved in heterochromatin condensation.

Discussion

In this work, we dissected the mechanisms of MeCP2 engagement with nucleosome^{601} and nucleosome^{satellite}, revealing its dual effects of consolidating or loosening nucleosome architecture. The binding of MeCP2 to naked DNA has been extensively investigated both *in vivo* and *in vitro*. However, the accurate DNA binding sites in genome still remains obscure, owing to intricate regulatory factors including DNA methylation status, DNA motifs, flanking sequences, and regional GC content. In contrast, binding events of MeCP2 on nucleosome are relatively stationary. MeCP2 preferentially localizes to SHL ± 6.5 as visualized in both nucleosomes, interacting with DNA gyres and acting as a lock to restrict

the dynamic entry/exit site and linker DNA. In spite of distinct binding modes, MeCP2 and H1 prompt similar consequence of linker DNA immobilization which facilitates chromatin condensation. Alternatively, stabilized nucleosome hinders the binding of transcription machinery, including chromatin remodeler, RNA polymerase and transcription factors, ultimately leading to gene repression. Conversely, MeCP2 occupied at SHL ± 1.5 distorts MeCP2 at SHL ± 6.5 and induces nucleosome unwrapping, giving rise to increased chromatin accessibility. Therefore, the positioning of MeCP2 plays dominant roles in regulating chromatin architecture.

Notably, whether MeCP2 localizes to SHL ± 1.5 is likely to be modulated by GC content. Alignment of DNA densities at SHL – 1.5 between free nucleosome^{satellite} and MeCP2-bound nucleosome^{satellite} revealed that MeCP2 engagement widened major groove (Extended Data Fig. 8d), similar to the effect of MeCP2 on naked DNA. However, nucleosomal DNA at SHL ± 1.5 is relatively rigid, preventing such DNA structure alternation. Consequently, MeCP2 is absent at SHL ± 1.5 in most nucleosomes. It is widely reported that low GC% sequences tend to form intrinsically dynamic nucleosomes[50], which are more susceptible to MeCP2-induced DNA distortion. We thus hypothesized that DNA dynamics conferred by low GC content are key for MeCP2 localization at SHL ± 1.5. Nevertheless, the principle governing MeCP2 localization at SHL ± 1.5 require further investigation.

In structures of MeCP2 complexed with naked DNA, residues R111 and R133 mediate base-specific recognition by forming hydrogen bonds with hydroxyl groups exposed in the DNA major groove. While interacting with nucleosomal DNA, we notice that at least one residue needs to bind hydroxyl group of DNA base. The other residue commonly contacts amino group as shown in 'TTC' and 'GA' motifs owing to the sequence constrain (Fig. 3c), providing weaker interaction force than that with hydroxyl group. Yet, additional connections with H3 compensate for reduced base-specific DNA interactions and contribute to strong nucleosome binding. Meanwhile, this finding accounts for the preferred nucleosome positions of MeCP2 at SHL ± 6.5 and SHL ± 1.5, all of which are proximal to H3.

As a nucleosome binding protein involved in chromatin condensation, the relationship between MeCP2 and H1 is extensively studied, however, with controversial conclusions. Single molecule study and ChIP-seq data suggested the co-binding of MeCP2 and H1 on the nucleosome and genome[24,35], yet cell-based assay supported the notion that MeCP2 competed with H1[5,37]. Our structures show separated occupation sites of MeCP2 and H1, allowing the spatial availability to bind on the same nucleosome. However, there are at least two factors influencing the co-existence of MeCP2 and H1. The primary factor is that some nucleosomes could be unwrapped by MeCP2, which triggers H1 eviction without linker DNA. Moreover, the linker DNA orientations in the nucleosomes bound by H1 and MeCP2 are varied, enabling one sturdy binding while destabilizing the other. The hypothesis is in good agreement with the single molecule assay that co-occupation of H1 to nucleosome reduces the stabilizing effect of MeCP2. Thus, MeCP2 and H1 are not generally coexistence or competition.

The gene repression by MeCP2 was initially attributed to the recruitment of NCoR/SMRT and HDAC co-repressor and the DNA methylation induced heterochromatin assembly. However, recent reports pointed that repressor function still maintained in the absence of

TRD and DNA methyltransferase, indicative of excess strategies. Our results clarify another manner that MeCP2 proteins bind at entry/exit sites on nucleosome to stabilize the dynamic linker DNA, assisting the heterochromatin compression. Collectively, our findings illustrate the unexpected binding mode of MeCP2 on nucleosome and delineate the atypical way of MeCP2 to regulate chromatin architecture which partially explains the abundant data of its gene repression and activation effects. This study fulfills the inadequate part of MeCP2 behavior on chromatin, providing more comprehensive framework to understand MeCP2 function.

References

1 Amir, R. E. et al. Rett syndrome is caused by mutations in X-linked MECP2, encoding methyl-CpG-binding protein 2. *Nature Genetics* **23**, 185-188 (1999).

2 Moretti, P. & Zoghbi, H. Y. MeCP2 dysfunction in Rett syndrome and related disorders. *Curr Opin Genet Dev* **16**, 276-281 (2006).

3 Liu, Y. et al. Exploring the complexity of MECP2 function in Rett syndrome. *Nature Reviews Neuroscience* **26**, 379-398 (2025).

4 Shahbazian, M. D. & Zoghbi, H. Y. Molecular genetics of Rett syndrome and clinical spectrum of MECP2 mutations. *Current Opinion in Neurology* **14**, 171-176 (2001).

5 Nan, X., Campoy, F. J. & Bird, A. MeCP2 is a transcriptional repressor with abundant binding sites in genomic chromatin. *Cell* **88**, 471-481 (1997).

6 Lewis, J. D. et al. Purification, sequence, and cellular localization of a novel chromosomal protein that binds to methylated DNA. *Cell* **69**, 905-914 (1992).

7 Ho, K. L. et al. MeCP2 binding to DNA depends upon hydration at methyl-CpG. *Molecular Cell* **29**, 525-531 (2008).

8 Bird, A. et al. Absence of MeCP2 binding to non-methylated GT-rich sequences in vivo. *Nucleic Acids Research* **48**, 3542-3552 (2020).

9 Chen, L. et al. MeCP2 binds to non-CG methylated DNA as neurons mature, influencing transcription and the timing of onset for Rett syndrome. *Proc Natl Acad Sci U S A* **112**, 5509-5514 (2015).

10 Clemens, A. W. *et al.* MeCP2 represses enhancers through chromosome topology-associated DNA methylation. *Molecular Cell* **77**, 279-293.e278 (2020).

11 Kinde, B., Wu, D. Y., Greenberg, M. E. & Gabel, H. W. DNA methylation in the gene body influences MeCP2-mediated gene repression. *Proceedings of the National Academy of Sciences* **113**, 15114-15119 (2016).

12 Lagger, S. et al. MeCP2 recognizes cytosine methylated tri-nucleotide and di-nucleotide sequences to tune transcription in the mammalian brain. *PLoS Genet* **13**, e1006793 (2017).

13 Yasui, D. H. et al. Integrated epigenomic analyses of neuronal MeCP2 reveal a role for long-range interaction with active genes. *Proceedings of the National Academy of Sciences* **104**, 19416-19421 (2007).

14 Baubec, T., Ivanek, R., Lienert, F. & Schubeler, D. Methylation-dependent and -independent genomic targeting principles of the MBD protein family. *Cell* **153**, 480-492 (2013).

15 Adams, V. H., McBryant, S. J., Wade, P. A., Woodcock, C. L. & Hansen, J. C. Intrinsic disorder and autonomous domain function in the multifunctional nuclear protein, MeCP2. *J Biol Chem* **282**, 15057-15064 (2007).
16 Ibrahim, A. et al. MeCP2 is a microsatellite binding protein that protects CA repeats from nucleosome invasion. *Science* **372** (2021).
17 Mellén, M., Ayata, P., Dewell, S., Kriaucionis, S. & Heintz, N. MeCP2 binds to 5hmC enriched within active genes and accessible chromatin in the nervous system. *Cell* **151**, 1417-1430 (2012).
18 Boxer, L. D. et al. MeCP2 represses the rate of transcriptional initiation of highly methylated long genes. *Molecular Cell* **77**, 294-309.e299 (2020).
19 Chahrour, M. et al. MeCP2, a key contributor to neurological disease, activates and represses Transcription. *Science* **320**, 1224-1229 (2008).
20 Cholewa-Waclaw, J. et al. Quantitative modelling predicts the impact of DNA methylation on RNA polymerase II traffic. *Proc Natl Acad Sci U S A* **116**, 14995-15000 (2019).
21 Liu, Y. et al. MECP2 directly interacts with RNA polymerase II to modulate transcription in human neurons. *Neuron* **112**, 1943-1958 e1910 (2024).
22 Nettles, S. A. et al. MeCP2 represses the activity of topoisomerase IIβ in long neuronal genes. *Cell Reports* **42** (2023).
23 Piccolo, F. M. et al. MeCP2 nuclear dynamics in live neurons results from low and high affinity chromatin interactions. *Elife* **8** (2019).
24 Chua, G. N. L. et al. Differential dynamics specify MeCP2 function at nucleosomes and methylated DNA. *Nat Struct Mol Biol* **31**, 1789-1797 (2024).
25 Ghosh, R. P. et al. Unique physical properties and interactions of the domains of methylated DNA binding protein 2. *Biochemistry* **49**, 4395-4410 (2010).
26 Lyst, M. J. et al. Rett syndrome mutations abolish the interaction of MeCP2 with the NCoR/SMRT co-repressor. *Nat Neurosci* **16**, 898-902 (2013).
27 Fuks, F. et al. The Methyl-CpG-binding protein MeCP2 links DNA methylation to histone methylation. *Journal of Biological Chemistry* **278**, 4035-4040 (2003).
28 Georgel, P. T. et al. Chromatin compaction by human MeCP2. Assembly of novel secondary chromatin structures in the absence of DNA methylation. *J Biol Chem* **278**, 32181-32188 (2003).
29 Koerner, M. V. et al. Toxicity of overexpressed MeCP2 is independent of HDAC3 activity. *Genes & Development* **32**, 1514-1524 (2018).
30 Wade, P. A. Methyl CpG-binding proteins and transcriptional repression. *Bioessays* **23**, 1131-1137 (2001).
31 Klose, R. J. et al. DNA binding selectivity of MeCP2 due to a requirement for A/T sequences adjacent to methyl-CpG. *Mol Cell* **19**, 667-678 (2005).
32 Sheikh, T. I., Harripaul, R., Ayub, M. & Vincent, J. B. MeCP2 AT-Hook1 mutations in patients with intellectual disability and/or schizophrenia disrupt DNA binding and chromatin compaction in vitro. *Hum Mutat* **39**, 717-728 (2018).
33 Tillotson, R. et al. Radically truncated MeCP2 rescues Rett syndrome-like neurological defects. *Nature* **550**, 398-401 (2017).

34 Nikitina, T. et al. MeCP2-chromatin interactions include the formation of chromatosome-like structures and are altered in mutations causing Rett syndrome. *J Biol Chem* **282**, 28237-28245 (2007).
35 Lee, W., Kim, J., Yun, J. M., Ohn, T. & Gong, Q. MeCP2 regulates gene expression through recognition of H3K27me3. *Nat Commun* **11**, 3140 (2020).
36 Wang, L. et al. Rett syndrome-causing mutations compromise MeCP2-mediated liquid-liquid phase separation of chromatin. *Cell Res* **30**, 393-407 (2020).
37 Skene, P. J. et al. Neuronal MeCP2 is expressed at near histone-octamer levels and globally alters the chromatin state. *Mol Cell* **37**, 457-468 (2010).
38 Ito-Ishida, A. et al. MeCP2 levels regulate the 3D structure of heterochromatic foci in mouse neurons. *The Journal of Neuroscience* **40**, 8746-8766 (2020).
39 Ghosh, R. P., Horowitz-Scherer, R. A., Nikitina, T., Shlyakhtenko, L. S. & Woodcock, C. L. MeCP2 binds cooperatively to its substrate and competes with histone H1 for chromatin binding sites. *Mol Cell Biol* **30**, 4656-4670 (2010).
40 Mishra, G. P. et al. Interaction of methyl-CpG-binding protein 2 (MeCP2) with distinct enhancers in the mouse cortex. *Nature Neuroscience* **28**, 62-71 (2024).
41 Rube, H. T. et al. Sequence features accurately predict genome-wide MeCP2 binding in vivo. *Nat Commun* **7**, 11025 (2016). https://doi.org/10.1038/ncomms11025
42 Zhou, B.-R. et al. Atomic resolution cryo-EM structure of a native-like CENP-A nucleosome aided by an antibody fragment. *Nature Communications* **10** (2019).
43 Zhou, B. R. et al. Distinct structures and dynamics of chromatosomes with different human linker histone isoforms. *Mol Cell* **81**, 166-182 e166 (2021).
44 Lei, M., Tempel, W., Chen, S., Liu, K. & Min, J. Plasticity at the DNA recognition site of the MeCP2 mCG-binding domain. *Biochim Biophys Acta Gene Regul Mech* **1862**, 194409 (2019).
45 Wen, Y. et al. MECP2 mutation spectrum and its clinical characteristics in a Chinese cohort. *Clin Genet* **98**, 240-250 (2020).
46 Dombrowski, M., Engeholm, M., Dienemann, C., Dodonova, S. & Cramer, P. Histone H1 binding to nucleosome arrays depends on linker DNA length and trajectory. *Nat Struct Mol Biol* **29**, 493-501 (2022).
47 Song, F. et al. Cryo-EM study of the chromatin fiber reveals a double helix twisted by tetranucleosomal units. *Science* **344**, 376-380 (2014).
48 Schalch, T., Duda, S., Sargent, D. F. & Richmond, T. J. X-ray structure of a tetranucleosome and its implications for the chromatin fibre. *Nature* **436**, 138-141 (2005).
49 Baker, S. A. et al. An AT-hook domain in MeCP2 determines the clinical course of Rett syndrome and related disorders. *Cell* **152**, 984-996 (2013).
50 Tillo, D., & Hughes, T. R. G+C content dominates intrinsic nucleosome occupancy. *BMC bioinformatics*, **10**, 442 (2009).

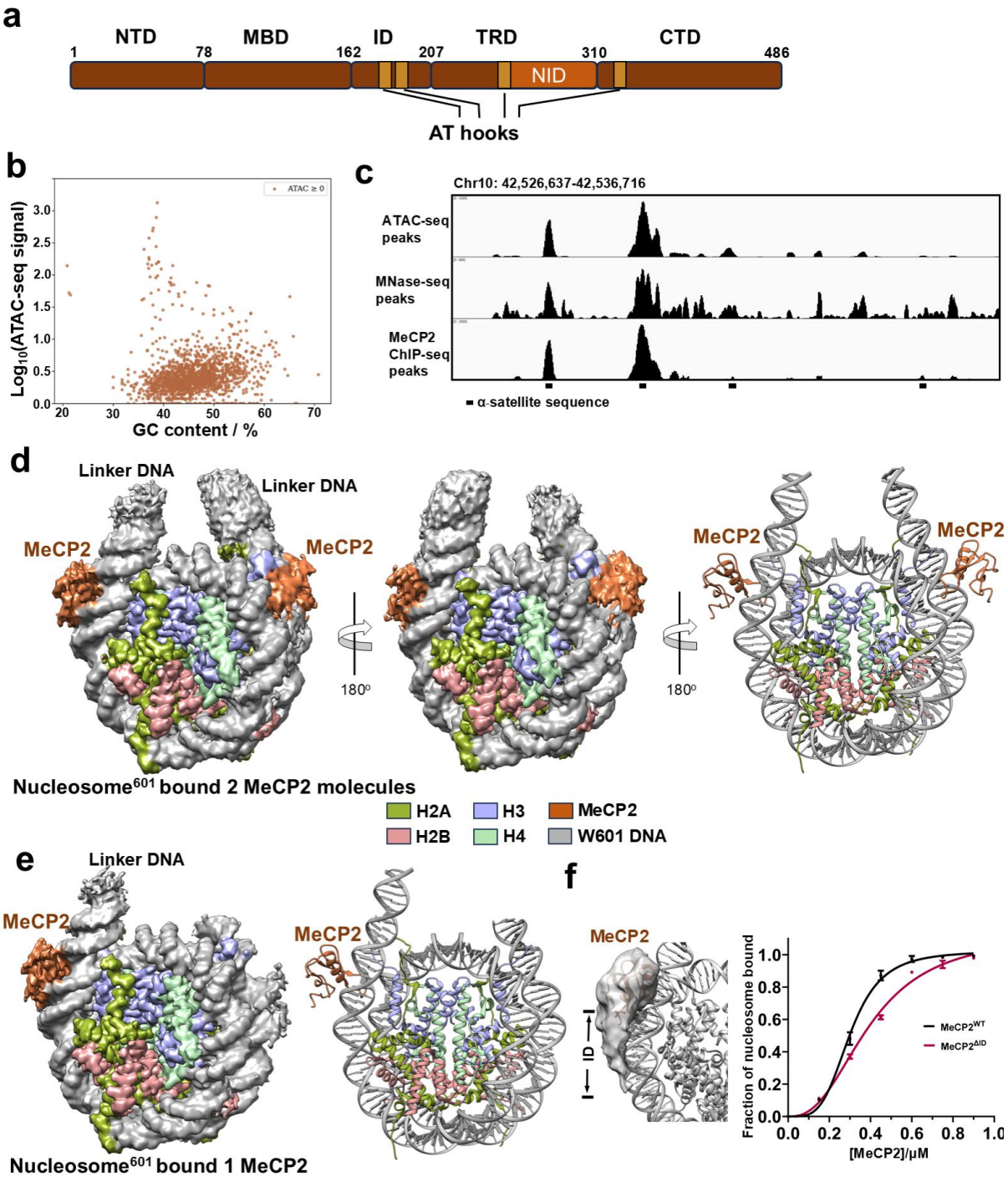
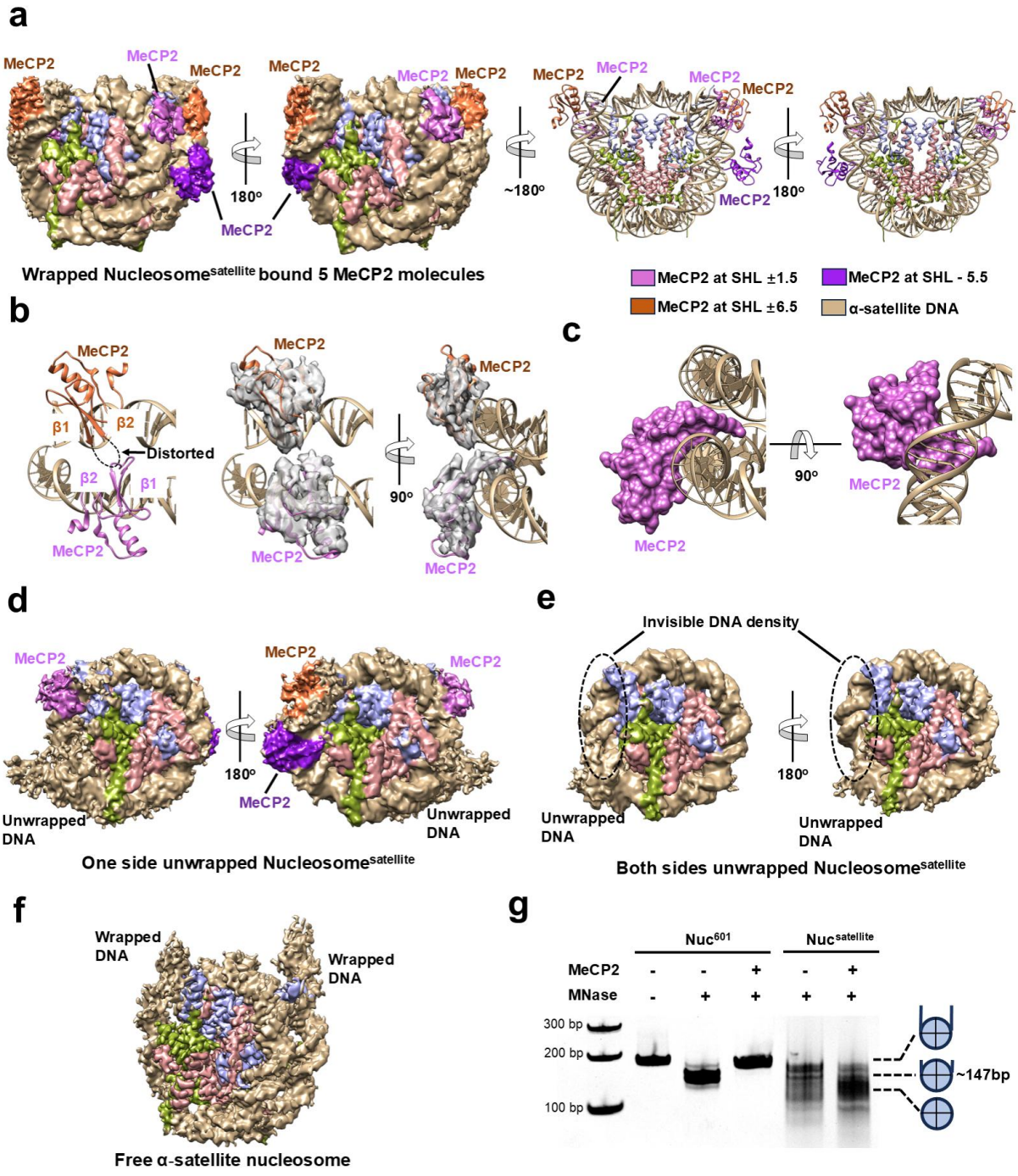


Fig. 1 | Chromatin accessibility analysis and structures of nucleosome^{601} complexed with MeCP2. a, Domain architecture of human MeCP2, with residue numbers indicating domain boundaries. AT hook domains are highlighted in yellow. **b,** Distribution of ATAC-seq signal with GC%. **c,** Representative tracks of MeCP2 ChIP-seq, MNase-seq and ATAC-seq data at α-satellite sequence locations. **d** and **e**, cryo-EM density maps and atomic models for nucleosome^{601} bound to two MeCP2 molecules (d) and one MeCP2 (e). MeCP2 located at SHL ± 6.5 are colored orange. ScFv was omitted for a clear visualization of nucleosome. **f,** Extended EM density corresponding to ID (left), and plots showing the bindings of WT MeCP2 (MeCP2^{WT}) and ID truncated MeCP2 (MeCP2$^{\Delta ID}$) to nucleosome^{601} (right). Apparent

420 K_D values are 0.29 ± 0.03 μM for $MeCP2^{WT}$, and 0.41 ± 0.03 μM for $MeCP2^{\Delta ID}$. The error
421 bars represent for standard deviations from three independent experiments.
422



423

424 **Fig. 2 | Cryo-EM structures of nucleosome^{satellite} complexed with MeCP2. a,** Two views
425 of the cryo-EM density maps (left) and corresponding atomic models (right) for the 177 bp α-
426 satellite nucleosome bound by five MeCP2 molecules. Map is lowpass filtered to 8 Å to
427 better visualize the MeCP2 densities. Two MeCP2 molecules are located at SHL ± 6.5 (dark
428 yellow), two molecules at SHL ± 1.5 (orchid), and one molecule at SHL − 5.5 (purple). ScFv
429 was omitted for a clear visualization of nucleosome. **b,** Zoomed-in structure showing conflict
430 between MeCP2 molecules at SHL − 1.5 and SHL + 6.5. EM density is shown in transparent
431 gray. Disordered L2 loop of MeCP2 at SHL + 6.5 is presented at black dash line. **c,** Insertion
432 of MeCP2 at SHL − 1.5 into DNA gyres. MeCP2 is displayed as orchid surface. **d,** Cryo-EM
433 density map of MeCP2 bound nucleosome^{satellite} with one entry/exit side unwrapped. Map is

lowpass filtered to 6 Å. **e,** Cryo-EM density map of MeCP2 bound nucleosome^{satellite} with both entry/exit sides unwrapped. Map is lowpass filtered to 6 Å. Invisible entry/exit side DNA densities are highlighted with black dash oval. **f,** Cryo-EM density map of free nucleosome^{satellite}. **g,** MNase digestion assay of the nucleosome^{601} and nucleosome^{satellite} in the presence and absence of MeCP2. Diagram of nucleosomes with protected long linker DNA (upper), no linker DNA (middle, ~147 bp) and deep digested nucleosomal DNA (lower) are shown at right side.

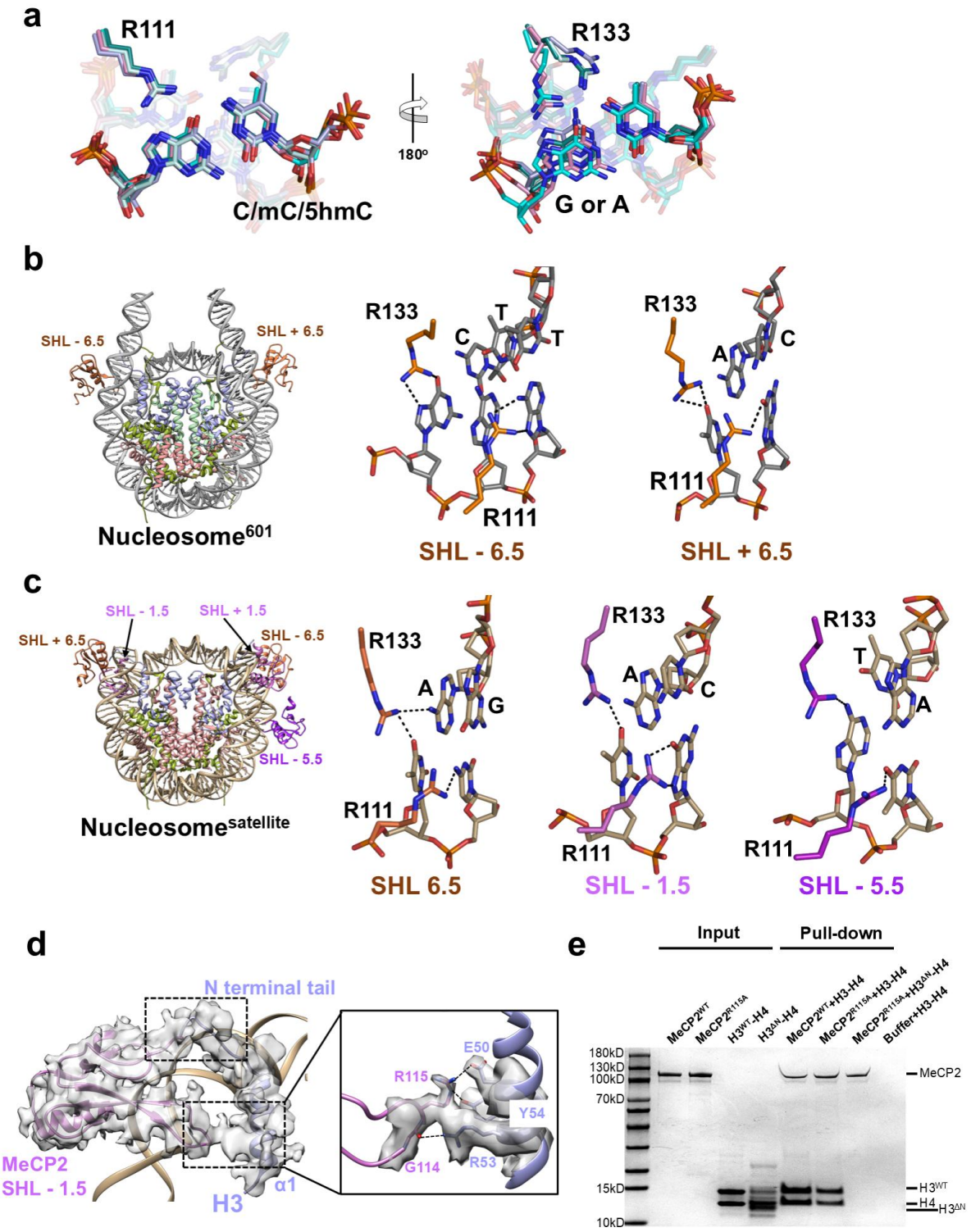


Fig. 3 | Structural analysis of the interactions between MeCP2 and nucleosomes. a, Structure alignments of MeCP2 R111 and R133 in MeCP2-DNA crystal structures. Structures are colored as follows: PDB 3C2I (cyan), 6OGJ (palecyan), 6OGK (forest), 6C1Y (pink), and 6YWW (light blue). **b** and **c,** Atomic models of nucleosome^{601} (b) and nucleosome^{satellite} (c) bound to MeCP2, showing hydrogen bonds (dash lines) between R111 and R133 of MeCP2 and nucleosomal DNA. Side chains are shown as sticks. **d,** Zoomed-in view of the interaction between MeCP2 bound at SHL −1.5 and histone H3, with transparent cryo-EM density superimposed for both molecules. Boxed regions indicate the magnified

interfaces, with key residues labelled. **e,** Pull-down assay showing WT and mutated MeCP2 proteins bind to WT and mutated H3-H4 tetramers.

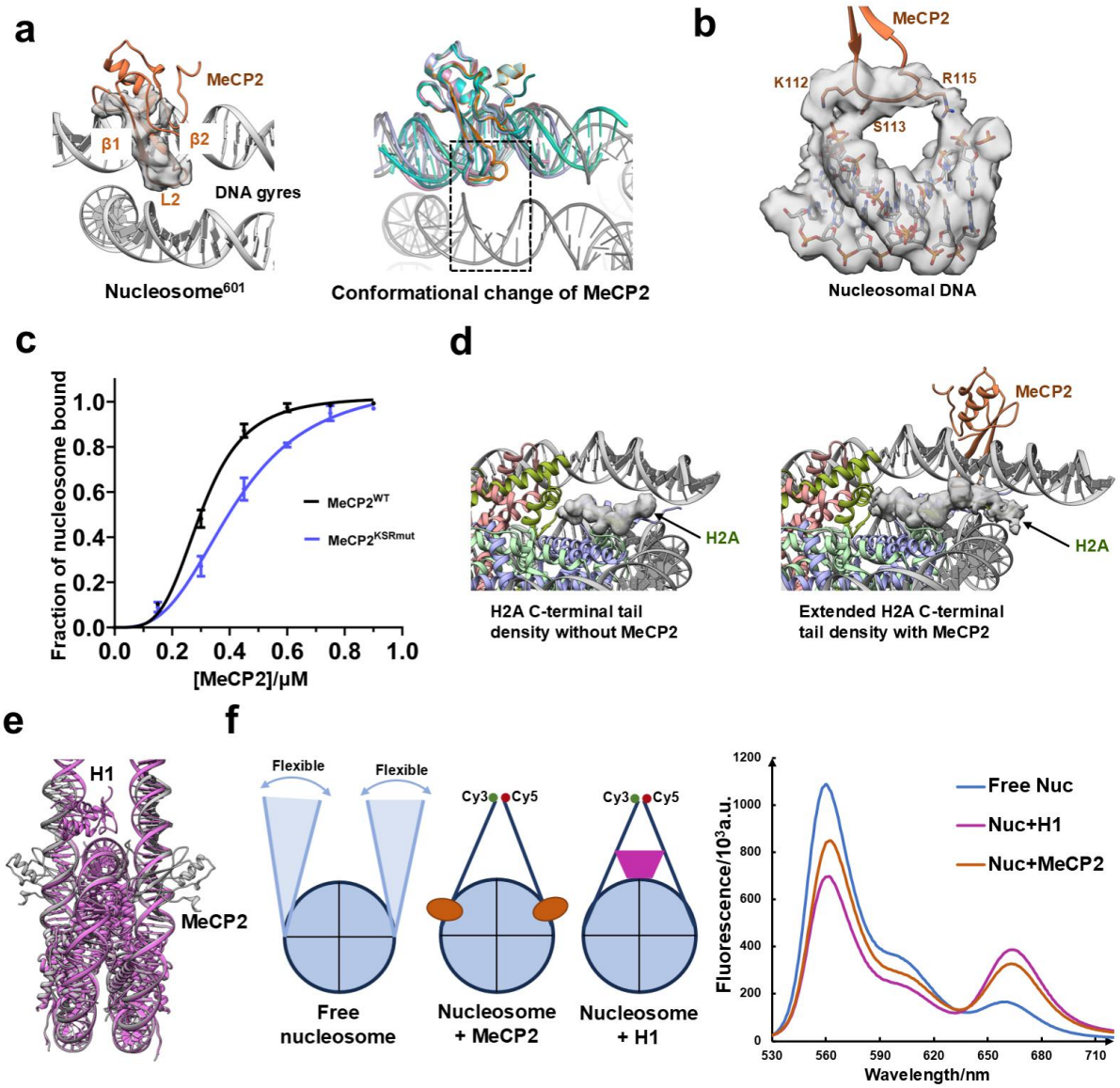


Fig. 4 | Nucleosome^{601} linker DNA compaction by MeCP2. a, Zoomed-in view of the MeCP2 L2 loop conformational change. Left: Cryo-EM density map of MeCP2. Right: structural alignment of MeCP2-nucleosome with MeCP2-DNA complexes (PDB 6OGJ: palecyan, 6OGK: forest, 6C1Y: pink, and 6YWW: light blue). The interaction between the loop and the neighboring nucleosomal DNA is indicated by the dashed rectangle. **b,** Atomic model of MeCP2 bound neighboring DNA, with key residues K112, S113 and R115 shown as stick. EM density is displayed in transparent gray. **c,** Plots of nucleosome^{601} binding to MeCP2^{WT} and MeCP2^{KSRmut}. The error bars represent for standard deviations from three independent experiments. Apparent K_D values 0.29 ± 0.03 μM for MeCP2^{WT}, and 0.42 ± 0.03 μM for MeCP2^{KSRmut} are obtained by fitting the data to the Hill equation. **d,** Cryo-EM density maps of the H2A C-terminal tail with and without MeCP2 engagement. **e,** Structural alignment of the nucleosome^{601} bound to H1 (magenta) and MeCP2 (gray). **f,** Left: schematic model of nucleosome linker DNA compaction by MeCP2 and H1. Right: FRET assay results. Nuc is short for nucleosome. The molar ratios of H1 or MeCP2 to nucleosome are: [H1]/[Nuc] = 1.5:1, [MeCP2]/[Nuc] = 3:1.

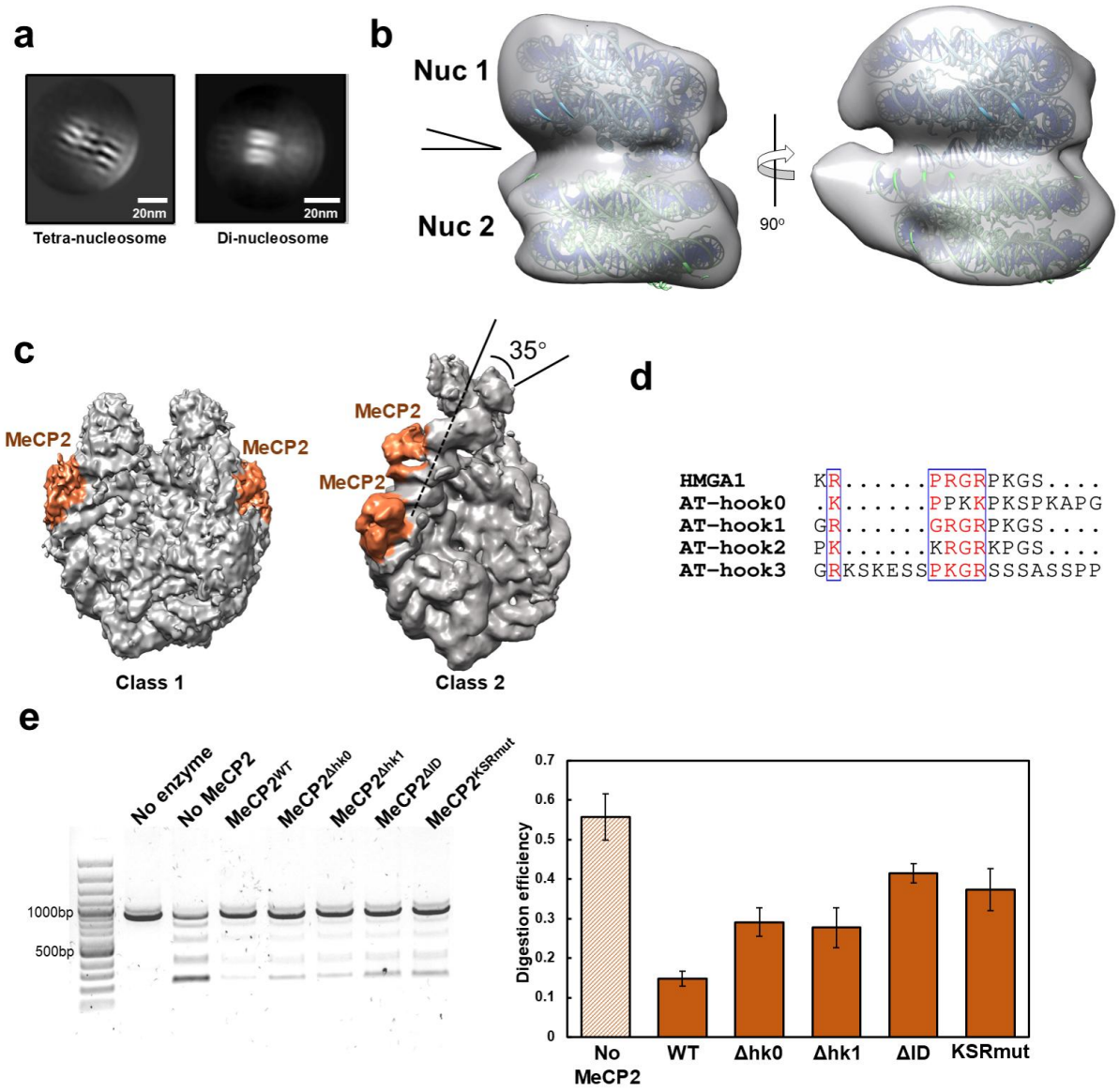


Fig. 5 | NA compaction by MeCP2. a, 2D class averages of representative tetra-nucleosome (left) and di-nucleosome (right) from EM data of MeCP2 bound NA. **b,** Two views of the di-nucleosome density map from MeCP2 bound NA data. Two nucleosome models are superposed into the map. Polygonal line represents for the tilt angle of two nucleosomes. **c,** Density map of nucleosomes engaged by two MeCP2 molecules bound at both entry/exit sites (left, class 1) and at the same entry/exit site (right, class 2), extracted from the MeCP2-bound NA data. Densities corresponding to MeCP2 are colored orange. **d,** Sequence alignment of four AT hook domains with HMGA1. **e,** Endonuclease cleavage assay of NA bound WT and mutated MeCP2 proteins. Right panel shows quantification of the digestion patterns. The error bars represent for standard deviations from three independent experiments.

Methods

Expression and purification of histones

Recombinant human histones H2A, H2B, H3, $H3^{\Delta N}$ (residues 1-38 truncated), H4 and H1.4 were expressed individually in Escherichia coli BL21(DE3) cells as described in a previous study[51]. All mutations in our study were generated using QuikChange kit (Transgen). Briefly, E. coli cells harboring each histone expression plasmid were grown at 37 °C in 2 x YTB Broth. When OD_{600} reached around 0.6-0.8, 0.5 mM IPTG was added to induce recombinant protein expression for 6 hrs at 37 °C. The cells were harvested and resuspended in 50 ml of buffer A (50 mM Tris-HCl, pH 8.0, 500 mM NaCl, 1 mM PMSF, 5% glycerol), followed by sonication on ice for 10 min with a pulse of 5 s on and 7 s off. The cell lysates were centrifuged at 18,000 rpm for 20 min at 4 ºC. The supernatant was discarded. The pellet containing histones was resuspended in 50 ml of buffer B (20 mM sodium acetate, pH 5.2, 100 mM NaCl, 5 mM DTT, 1 mM EDTA, and 7 M urea). The samples were rotated for 12 hrs at room temperature, and the supernatant was recovered by centrifugation at 20,000 rpm for 60 min at 4 ºC. The supernatant was loaded to Hitrap S column chromatography (Cytiva). The column was washed with buffer B, and histone protein was eluted by a linear gradient of 100 to 800 mM NaCl. The purified histones were dialyzed against water for three times, and freeze-dried.

Expression and purification of MeCP2

The plasmid pET30a containing the human full length MeCP2, $MeCP2^{R115A}$, $MeCP2^{KSRmut}$ (K112A, S113A and R115A), $MeCP2^{\Delta hk0}$ (residues 171-180 truncated), $MeCP2^{\Delta hk1}$ (residues 186-192 truncated), $MeCP2^{\Delta ID}$ (residues 171-192 truncated) with an MBP-tag at N-terminus and His-tag at the C-terminus were cloned using NotI and EcoRI restriction sites. The plasmids harboring the above constructions were transformed into BL21(DE3) cells and grown in LB medium. When OD_{600} reached 0.8, 0.5 mM IPTG was added to induce protein expression at 18 ºC for 16 hrs. Cells were harvested and resuspended in the buffer containing 20 mM HEPES, pH 7.0, 1 M NaCl, 0.5 mM TCEP and protease inhibitor cocktail (Roche). After sonification and ultracentrifuge, the supernatant went through Nickle affinity beads (Cytiva). The column was washed by the buffer containing 20 mM HEPES, pH 7.0, 1 M NaCl, 0.5 mM TCEP, 80 mM imidazole, then eluted by the buffer containing 20 mM HEPES pH 7.0, 1 M NaCl, 0.5 mM TCEP, 250 mM imidazole. The solution containing the target protein was concentrated to ~0.5 ml and went through gel filtration on Superdex 200 10/300 increase column (Cytiva) equilibrated with buffer containing 20 mM HEPES pH 7.0, 200 mM NaCl, 0.2 mM TCEP.

Preparation of DNA

Short DNA fragments used for mono-nucleosome reconstruction were prepared by PCR amplification, followed by ethanol precipitation and purification using the POROS column. 187 bp W601 DNA used for structural study was treated by CpG methyltransferase M.SssI (New England Biolabs) before mono-nucleosome reconstruction. The 187 bp W601 sequence is shown below:

GGACCCTATACGCGGCCGCCCTGGAGAATCCCGGTGCCGAGGCCGCTCAAT
TGGTCGTAGACAGCTCTAGCACCGCTTAAACGCACGTACGCGCTGTCCCCCGCGT
TTTAACCGCCAAGGGGATTACTCCCTAGTCTCCAGGCACGTGTCAGATATATACA
TCCTGTGCATGTATTGAACAGCGACC

The 177 bp α-satellite sequence is shown below:

ATTGAGGCCTTCGTTGGAAACGGGATTTCTTCATTTCATGCTAGACAGAAGA ATTCTCAGTAACTTCTTTGTGCTGTGTGTATTCAACTCACAGAGTGGAACGTCCCT TTGCACAGAGCAGATTTGAAACACTCTTTTTGTGGAATTTGCAAGTGGAGATTTC AGCCGCTTTGAGAA.

Briefly, The PCR products were pelleted by 75% ethanol containing 0.3 M NaAc at pH 5.2. The sample was incubated for 120 min at -20 ºC, followed by centrifugation. The supernatants were discarded, and the pellet was resuspended by TE buffer. The sample was loaded to POROS column chromatography (Thermo Fisher). The column was washed with buffer containing 20 mM Tris-HCl, pH 7.5 ,1 mM EDTA, and the DNA was eluted by a linear gradient of 0 to 2 M NaCl. The purified DNA were collected and stored at 4 ºC. All DNA fragments were prepared and purified with the same procedure.

For 4 × 197 bp and 6 × 197 bp W601 nucleosome array (NA) DNA preparation, Escherichia coli TransStbl3 Cell (TransGen) transfected with plasmids containing the W601 repeats were grown and prepared using LB medium in 37℃ for 16 hrs. Large scale preparation and purification of the plasmid followed previous protocol[51]. Purified plasmids were digested with EcoRV (Takara) overnight, and purified by stepwise PEG 6000 precipitation.

Reconstitution of nucleosomes and nucleosome arrays

Purified recombinant histones were mixed at equimolar ratios and dialyzed against refolding buffer (25 mM Tris-HCl, pH 8.0, 1 mM EDTA, 1 mM DTT, and 2 M NaCl) for approximately 16 hrs. The mixture was centrifuged at 13,000 rpm to remove any insoluble material. Soluble octamers were purified by size fractionation on a Superdex 200 10/300 increase gel filtration column. Purified histone octamers and DNA were mixed with a 1.4:1 ratio in high-salt buffer (2 M NaCl, 20 mM Tris-HCl, pH 8.0, 1 mM EDTA, 1 mM DTT). Mixture in a dialysis bag was placed in 600 mL of the high-salt buffer and dialyzed for 30 min followed by salt gradient dialysis. 3 L of a low-salt buffer (100 mM NaCl, 20 mM Tris-HCl, pH 8.0, 1 mM EDTA, 1 mM DTT) were gradually pumped into dialysis buffer with a flow rate of 2 ml/min for 18 hrs. The dialysis bag was then dialyzed against low-salt buffer for 30 min. The dialysis was done at 4℃. The sample was then incubated at 37 ºC for 3-5 hrs. The mixture was centrifuged at 13,000 rpm to remove any insoluble material. The nucleosomes were further purified by ion-exchange chromatography (TSKgel DEAE, TOSOH Bioscience, Japan) to remove free DNA. The purified nucleosomes were dialyzed against buffer containing 20 mM HEPES, pH 7.0, 1 mM DTT. The purified 4 × 197 bp DNA and 6 × 197 bp DNA were used for nucleosome repeats reconstitution following the same procedure as mono-nucleosome. NAs were reconstituted by mixing nucleosome repeats with MeCP2. 4 × 197 bp NA was used for structural study, and 6 × 197 bp NA was used for endonuclease cleavage assay.

Cryo-EM sample preparation and data collection

For free nucleosome sample, 3 μM nucleosome was used for sample preparation. For MeCP2-nucleosome complexes, 3 μM nucleosome^{601} or nucleosome^{satellite} was mixed with 9 μM scFv , and 18 μM MeCP2. For 4 × 197 bp NA sample, 0.5 μM tetra-nucleosome was mixed with 10 μM MeCP2. Final 0.01% glutaraldehyde was applied to 4 × 197 bp NA complexed with MeCP2 5 min before grids freezing. The samples were incubated on ice for 30 min and then loaded onto the glow-discharged holey carbon grid (Quantifoil 300 mesh Cu R1.2/1.3 for free nucleosome and MeCP2 complexed with mono-nucleosome, Lacey holey grids 300 mesh for NA sample). All the grids were blotted for 4 s at 16 °C and 100% relative

humidity using a Vitrobot Mark IV plunger (Thermo Fisher) before being plunge-frozen in liquid nitrogen-cooled liquid ethane. Cryo-EM data were collected using JEOL CRYO ARM 300 II (JEOL) and Titan Krios G3 electron microscope (Thermo-Fisher) operated at 300kV. Micrographs were acquired in super-resolution mode using a 20-eV slit post-GIF Gatan K3 camera. The dose rate on the camera was set to 50 $e^-/Å^2$. The total exposure time of each micrograph was 4 s fractionated into 50 frames with 0.08 s exposure time for each frame. The data collection was automated using the SerialEM software package[52]. A total of 2,935 micrographs were collected for nucleosome^{601} complexed with scFv and MeCP2, 523 micrographs were collected for free nucleosome^{satellite}. 4,699 micrographs were collected for nucleosome^{satellite} complexed with scFv and MeCP2, and 6,670 micrographs were collected for tetra-nucleosome and MeCP2 complex.

Cryo-EM data processing

The data processing procedures were shown in Extended Data Fig. 2 for nucleosome^{601} bound MeCP2; Extended Data Fig. 4 for nucleosome^{satellite} bound MeCP2; Extended Data Fig. 6 for free nucleosome^{satellite}; and Extended Data Fig. 7 for NA sample. All 4 datasets were processed in RELION/5.0.1 and cryoSPARC v5.0 following the standard procedures[53,54]. The beam-induced image drift was corrected using Patch Motion Correction, followed by Patch CTF Estimation. Particles were automatically picked by Blob picker, and the generated 2D class averages were used for Template picker.

For MeCP2 bound nucleosome^{601} dataset, 2,198,708 particles were picked, and 1,382,105 particles selected after 2D classification were re-extracted without binning. Particles were transferred to RELION for 3D classification, 1 class with good density of nucleosome was selected and 839,676 particles re-extracted. Further 3D classification with finer angular sampling rate were performed. 2 classes of nucleosome bound 2 MeCP2 molecules and nucleosome bound 1 MeCP2 were selected and particles were transferred to cryoSPARC for CTF refinement and non-uniform refinement, generating 2.8 Å map for nucleosome bound 2 MeCP2 molecules and 3.0 Å map for nucleosome bound 1 MeCP2. Class of nucleosome bound 2 MeCP2 molecules was further submitted to 3D classification without alignment, and 1 class with extended ID domain was visualized.

302,816 particles were picked for free nucleosome^{satellite} dataset. Bad particles were removed by 2D classification and 37,579 particles were re-extracted and submitted to Abi-initial Reconstruction. 27,126 particles with high resolution nucleosome feature were selected for non-uniform refinement, and a final 3 Å map was generated.

For MeCP2 bound nucleosome^{satellite} dataset, 1,763,152 particles were picked from 4,699 micrographs. Bad particles were removed from 2D classification and 333,096 particles were selected and re-extracted. Abi-initial Reconstruction produced 1 good nucleosome class containing 210,880 particles, followed by 3D viability generating 4 classes with different conformations. After non-uniform refinement, 2.9 Å map was generated for wrapped nucleosome^{satellite} bound 5 MeCP2 molecules, 2.8 Å map was generated for wrapped nucleosome^{satellite} bound 3 MeCP2 molecules, 2.8 Å map was generated for one side unwrapped nucleosome^{satellite}, 2.8 Å map was generated for two sides unwrapped nucleosome^{satellite}.

Data processing of tetra-nucleosome bound MeCP2 was executed in RELION. For initial particle extraction with 4 x binning, 120 box size was used to separated tetra-nucleosome particles, 100 box size was used for di-nucleosome classification and 80 box size

was used for mono-nucleosome processing. 92,832 particles with tetra-nucleosome feature were selected, however, no reasonable 3D reconstructions were created. For di-nucleosome processing, 226,541 particles were selected after 2D classification, and 3D classification yield 2 classes without obvious disparity, possibly due to the low resolution. Thus, particles from 2 classes were combined and submitted to 3D auto-refine, generating a map with clear identified 2 nucleosomes. For mono-nucleosome reconstruction, 410,269 particles were selected and re-extracted after 2D classification, and 3D classification produced 2 classes with nucleosome bound MeCP2. One class containing nucleosome bound 2 MeCP2 molecules at SHL ± 6.5, in which the MeCP2 location is identical with that in nucleosome^{601}-scFv-2 MeCP2 molecules. The other class contained nucleosome with 2 MeCP2 molecules bound at the same entry/exit site.

Model building and structure analysis

For the nucleosome^{601}-scFv-2 MeCP2 molecules, an initial model of the nucleosome histone octamer and scFv was generated using the nucleosome structure (PDB: 8SYP). An initial model of the MeCP2 was generated from crystal structure of MeCP2-DNA (PDB: 6OGJ). The models were fitted into the cryo-EM density map, and the DNA sequence was built into the map from scratch in COOT[55] and the histone octamer and scFv were optimized by manual rebuilding. The whole complex was refined using real space refinement in PHENIX[56].

For the nucleosome^{satellite}-scFv-5 MeCP2 molecules and nucleosome^{satellite}-scFv-3 MeCP2 molecules, structure of nucleosome^{601}-scFv-2 MeCP2 molecules was used as initial model. Histone octamer and scFv were fitted into the map and manually rebuilt in COOT, and DNA was completely built in COOT. The model was refined using real space refinement in PHENIX. All the structure figures were made using UCSF Chimera[57] and PyMOL (Version 1.8, Schrödinger, LLC. DeLano Scientific).

Electrophoretic mobility shift assay

Nucleosomes at a final concentration of 0.3 μM were mixed with WT and mutated MeCP2 proteins at different concentration. Typical binding reactions of complex formation between protein and nucleosomes were carried out for 30 min on ice in buffer containing 20 mM HEPES, pH 7.3, 150 mM NaCl, and 0.5 mM TCEP. 5 μl of the binding reactions were analyzed on 4% or 5 % acrylamide gels in 0.2 x TBE at 120 V for 60 minutes at 4 °C. After electrophoresis, gels were stained with Super Red dye (Biosharp) and quantified using Image J. Binding data were fitted with the Hill equation and analyzed in Prism (Graphpad). Three independent experiments were performed.

MNase digestion assay

187 bp W601 nucleosome and 177 bp α-satellite nucleosome were used in this assay. MeCP2 was mixed with 200 ng nucleosomes with a molar ratio of 4:1 in 10 μl reaction system in buffer 20 mM HEPES, pH 7.0, 150 mM NaCl and 0.5 mM TCEP. After 10 min incubation on ice, 1 μl MNase reaction buffer and 0.5 U MNase (New England Biolabs) were added into the system. The mixture was placed into 37 °C incubator for 15 min. Purple gel loading dye (New England Biolabs) was added to stop the enzyme digestion reaction. And 3 μl of Phenol: Chloroform: isoamyl alcohol (25:24:1) was added into the solution to extract MeCP2 and histones. After centrifugation at 10,000 rpm for 2 min, supernatant was aspirated and analyzed on 6 % acrylamide gels in 0.2 x TBE at 120 V for 60 minutes at 4 °C. After

electrophoresis, gels were stained with Gel Red DNA dye (Biosharp). Three independent experiments were performed.

FRET assay

DNA fragment with fluorescent dyes labelled at both ends was produced using PCR by the Cy3 and Cy5 labeled primers. Nucleosome was reconstituted through the same procedure as unlabeled DNA. MeCP2 or H1.4 was titrated into 200 nM nucleosome in buffer 20 mM HEPES, pH 7.0, 100mM NaCl, 0.2mM TCEP. The fluorescence intensity was recorded using QuantaMaster from Photon Technology International. Excitation wavelength was set to 510 nm, and emission spectra were collected between 530nm ~ 730nm. Three independent experiments were performed.

Pull-down assay

Purified H3 or $H3^{\Delta N}$ and H4 in equal stoichiometric ratio were dissolved in ~1 ml unfolding buffer (7 M guanidine-HCl, 20 mM Tris-HCl, pH 7.4, 10 mM DTT) and were dialyzed against refolding buffer (10 mM Tris-HCl, pH pH 7.4, 1 mM EDTA, 1 mM DTT, 2 M NaCl) for about 12 hrs. The mixture was centrifuged at 13,000 rpm to remove any insoluble material. H3-H4 tetramer was purified by size fractionation on a Superdex 200 10/300 increase gel filtration column. Wild type and mutated H3-H4 tetramer were step-by-step diluted into reaction buffer (20 mM HEPES 7.0, 250 mM NaCl, 0.5 mM TCEP, 20 mM Imidazole). Equal molar of MeCP2 or $MeCP2^{R115A}$ were used to mix with diluted H3-H4 tetramer. After incubation on ice for 30 min, the reaction mixtures were added into washed HisPur Ni-NTA resin (Thermo Fisher) and agitated for 15 min at cold room. The mixtures were centrifuged to collect the resin, and supernatant was discarded. The resin was then washed twice by reaction buffer, and eluted using reaction buffer containing 250 mM Imidazole. Eluted samples were analyzed on SDS-PAGE.

Endonuclease cleavage assay of NA

A total of 1 μg of 6 × 197 bp hexa-nucleosome was incubated with WT MeCP2 or the mutants including $MeCP2^{\Delta hk0}$, $MeCP2^{\Delta hk1}$, $MeCP2^{\Delta ID}$ and $MeCP2^{KSRmut}$ at a molar ratio of 8:1 in FuniCut buffer at room temperature. Subsequently, 0.8 U of the restriction enzyme SmaI (Yeasen) was added to hexa-nucleosome with and without MeCP2. Samples were incubated at 37 °C for 15 min. The reactions were then mixed with Phenol: Chloroform: Isoamyl alcohol (25:24:1) at a 1:1 (v/v) ratio and vortexed to extract proteins. Following centrifugation, the supernatant was collected and loaded onto a 1% agarose gel stained with Super Red dye (Biosharp). Electrophoresis was performed in 1× TAE buffer at 110 V for 35 min. Three independent experiments were performed. Band intensities of the digestion products were quantified using ImageJ. Relative digestion was calculated as the ratio of product intensity in the presence of MeCP2 to that in its absence.

Processing of MeCP2-Associated Multi-Omics Sequencing Data

Raw FASTQ reads from MeCP2 ChIP-seq (GSE117508), MNase-seq (GSE117870) and ATAC-seq (GSE117507)[58,59] were preprocessed with fastp for adapter trimming and low-quality base filtering. Clean reads were mapped to the hg19 human reference genome via BWA-MEM, and PCR duplicates were removed using samtools markdup. MACS2 was used for peak calling with a P-value cutoff of 0.001. High-confidence MeCP2 peaks were retrieved as overlaps between ChIP-seq and MNase-seq peaks by bedtools intersect. We calculated interval-wise GC content and extracted normalized ATAC-seq signal from bigWig files with bedtools map, removing peaks with extreme GC values or missing signals. ATAC signals

were $\log_{10}(x+1)$-transformed to correct skewed distribution, and scatter plots were generated in Python (Matplotlib, SciPy) and saved as vector PDFs.

Methods References

51 Lian, T., Guan, R., Zhou, B.R. & Bai, Y. Structural mechanism of synergistic targeting of the CX3CR1 nucleosome by PU.1 and C/EBPα. *Nat Struct Mol Biol.* **31**, 633–643 (2024).

52 Mastronarde, D. N. Automated electron microscope tomography using robust prediction of specimen movements. *J. Struct. Biol.* **152**, 36–51 (2005).

53 Burt, A. et al. An image processing pipeline for electron cryo-tomography in RELION-5. *FEBS Open Bio.* **14**, 1788–1804 (2024).

54 Punjani, A., Rubinstein, J. L., Fleet, D. J. & Brubaker, M. A. cryoSPARC: algorithms for rapid unsupervised cryo-EM structure determination. *Nat. Methods.* **14**, 290–296 (2017).

55 Emsley, P., Lohkamp, B., Scott, W. G. & Cowtan, K. Features and development of Coot. Acta Crystallogr. *D Biol. Crystallogr.* **66**, 486–501 (2010).

56 Adams, P. D. et al. PHENIX: a comprehensive Python-based system for macromolecular structure solution. Acta Crystallogr. *D Biol. Crystallogr.* **66**, 213–221 (2010).

57 Pettersen, E. F. et al. UCSF Chimera—A visualization system for exploratory research and analysis. *J. Comput. Chem.* **25**, 1605–1612 (2004).

58 Xiang, Y. et al. Dysregulation of BRD4 function underlies the functional abnormalities of MeCP2 mutant neurons. *Mol. Cell.* **79**, 84–98.e89 (2020).

59 Harwood, J. C., Kent, N. A., Allen, N. D. & Harwood, A. J. Nucleosome dynamics of human iPSC during neural differentiation. *EMBO Rep.* **20**, (2019).

Data availability

The cryo-EM reconstructions and atomic models have been deposited in the Electron Microscopy Data Bank and the Protein Data Bank under the following accession codes: EMD-81860 and PDB ID 43GG for nucleosome^{601}-scFv-2 MeCP2 molecules; EMD-81890 for nucleosome^{601}-scFv-1 MeCP2 molecule; EMD-81894 for nucleosome^{601}-scFv-2 MeCP2 molecules with extended ID domain; EMD-81870 and PDB ID 43GQ for nucleosome^{satellite}-scFv-5 MeCP2 molecules; EMD-81871 and PDB ID 43GR for nucleosome^{satellite}-scFv-3 MeCP2 molecules; EMD-81876 for nucleosome^{satellite}-scFv-MeCP2 with one side unwrapped; EMD-81878 for nucleosome^{satellite}-scFv-MeCP2 with both sides unwrapped; EMD-81873 for free nucleosome^{satellite}; EMD-81899 for Di-nucleosome^{601} from 4 × 197 bp W601 NA; EMD-81891 for nucleosome^{601}-MeCP2 with 2 MeCP2 molecules at two entry/exit sites from NA sample; EMD-81898 for nucleosome^{601}-MeCP2 with 2 MeCP2 molecules at the same entry/exit site from NA sample.

Acknowledgments

We thank Dr. Yawen Bai and Dr. Bing-rui Zhou for providing the scFv and histones plasmids. We thank Dr. Yawen Bai for the helpful comments and advice. We thank Dr. Yong

Feng and Cryo-EM core facility in the Institute of Artificial Intelligence Biomedicine, Nanjing University for assistance in cryo-EM sample screening and data collection.

Funding

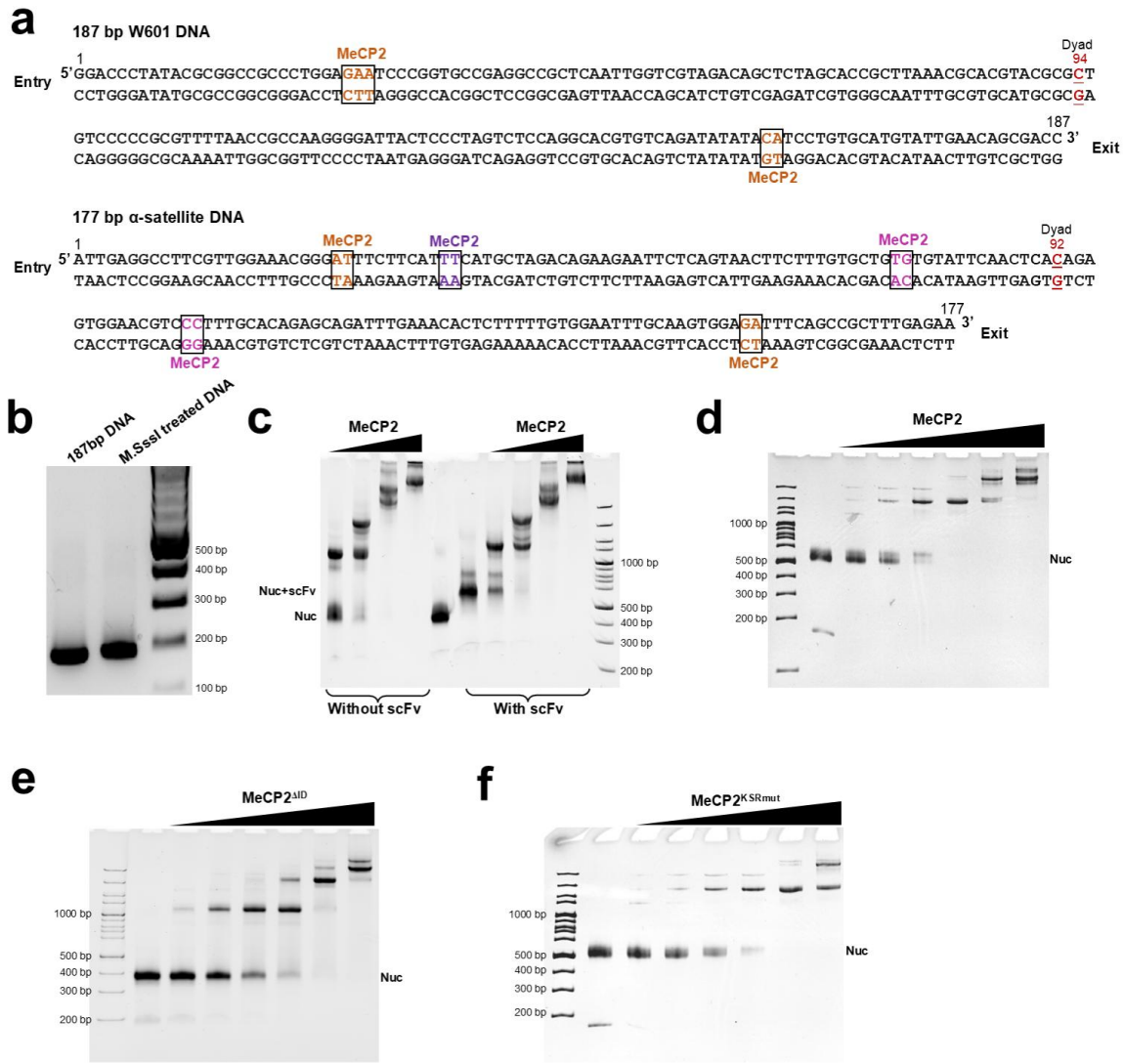
This research was supported by China Pharmaceutical University and Nanjing University. This work was supported by grants from National Natural Science Foundation of China grant (No. 82504676 for T.L., No. 3250040547 for R.G.)

Author contributions:

T.L. and R.G. conceptualized the work. T.L. and R.G. acquired funding. T.L., R.G., R.R., W.J., Y.W, Q.Y. administered the project. T.L. and R.G. supervised the work. T.L. and R.G. wrote the original draft, which was reviewed and edited by R.R., W.J., Y.W. and Q.Y..

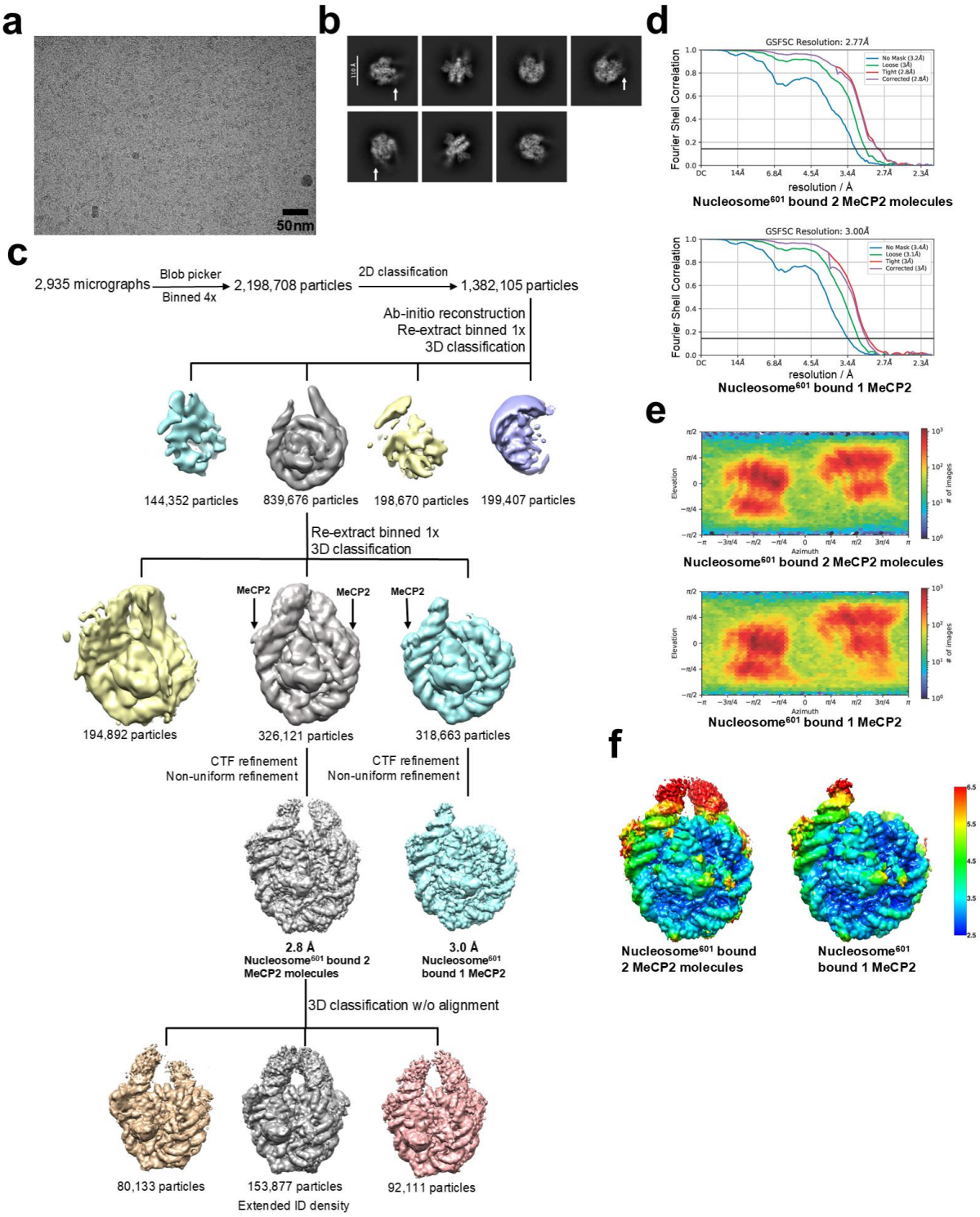
Competing interests

The authors declare no competing interests.

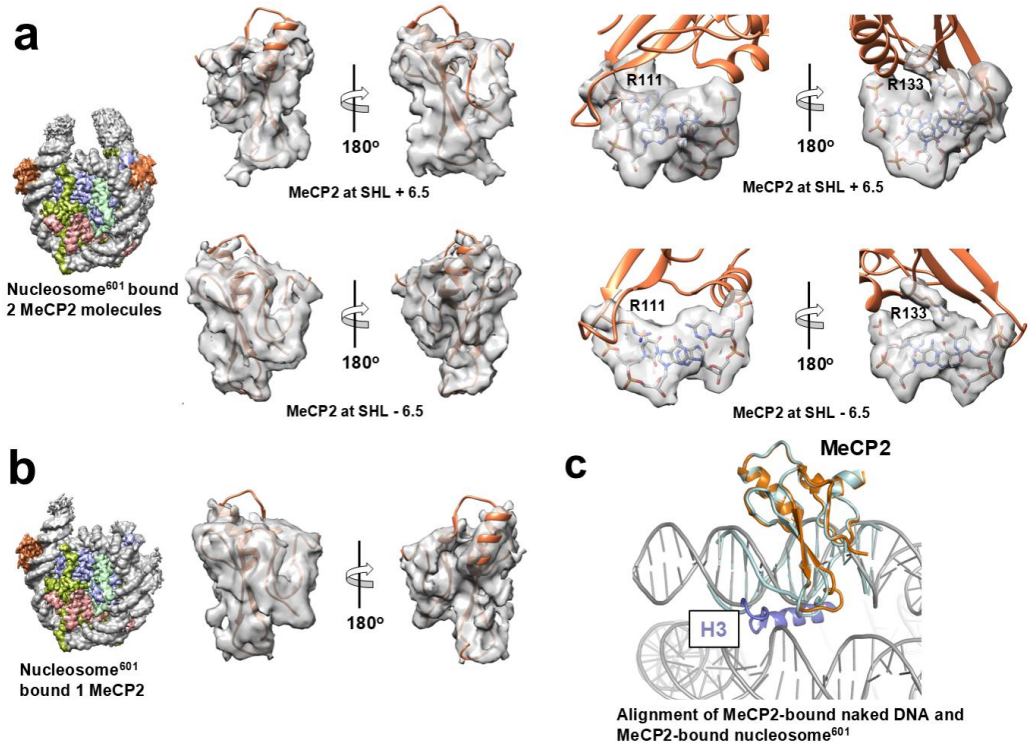


763

764 **Extended Data Fig. 1 | Characterization of MeCP2 binding to nucleosomes. a,** Sequences
765 of the 187 bp W601 and 177 bp α-satellite DNA sequences. MeCP2-binding motifs are
766 boxed. The base pairs at dyad are underlined. **b,** 187 bp W601 DNA verification after M.SssI
767 treatment. **c**, Comparison of nucleosome^{601} (Nuc) bound MeCP2 with and without scFv.
768 Molar ratios of [MeCP2]/[Nuc] are 1:1, 2:1, 3:1 and 4:1. **d** to **f**, EMSAs of the nucleosome^{601}
769 with MeCP2 (d), MeCP2$^{\Delta ID}$ (e) and MeCP2^{KSRmut} (f) titrated at molar ratios ([protein]/[Nuc])
770 of 0.5:1, 1:1, 1.5:1, 2:1, 2.5:1 and 3:1. The nucleosome concentration was held constant at 0.3
771 μM.
772



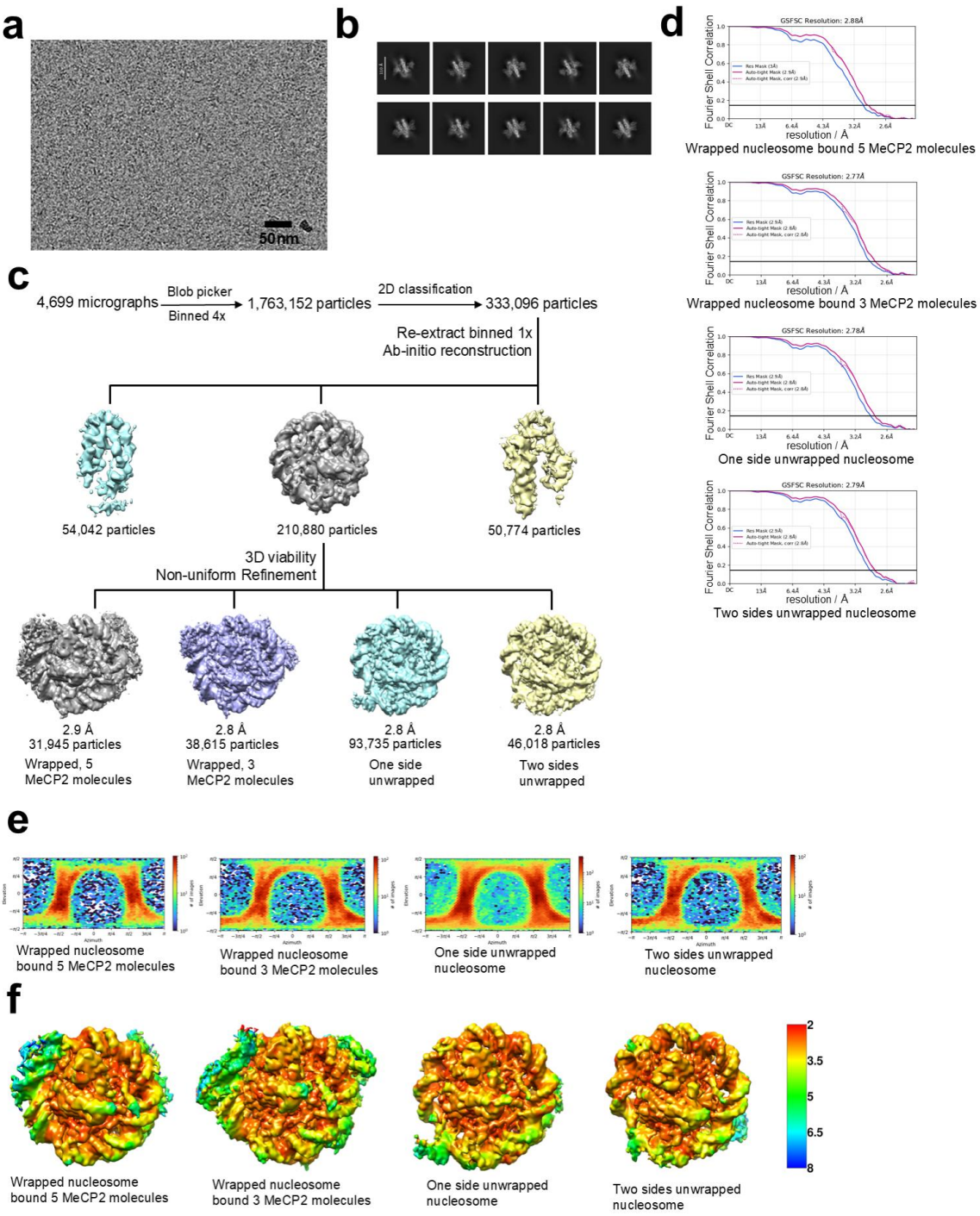
Extended Data Fig. 2 | Data processing for 187 bp W601 nucleosome bound to MeCP2. **a,** Raw image. **b,** 2D classification results. Arrows indicate the presence of MeCP2. **c,** Particle analysis. **d,** FSC curves. **e,** Particle orientation distribution. **f,** Local resolution.



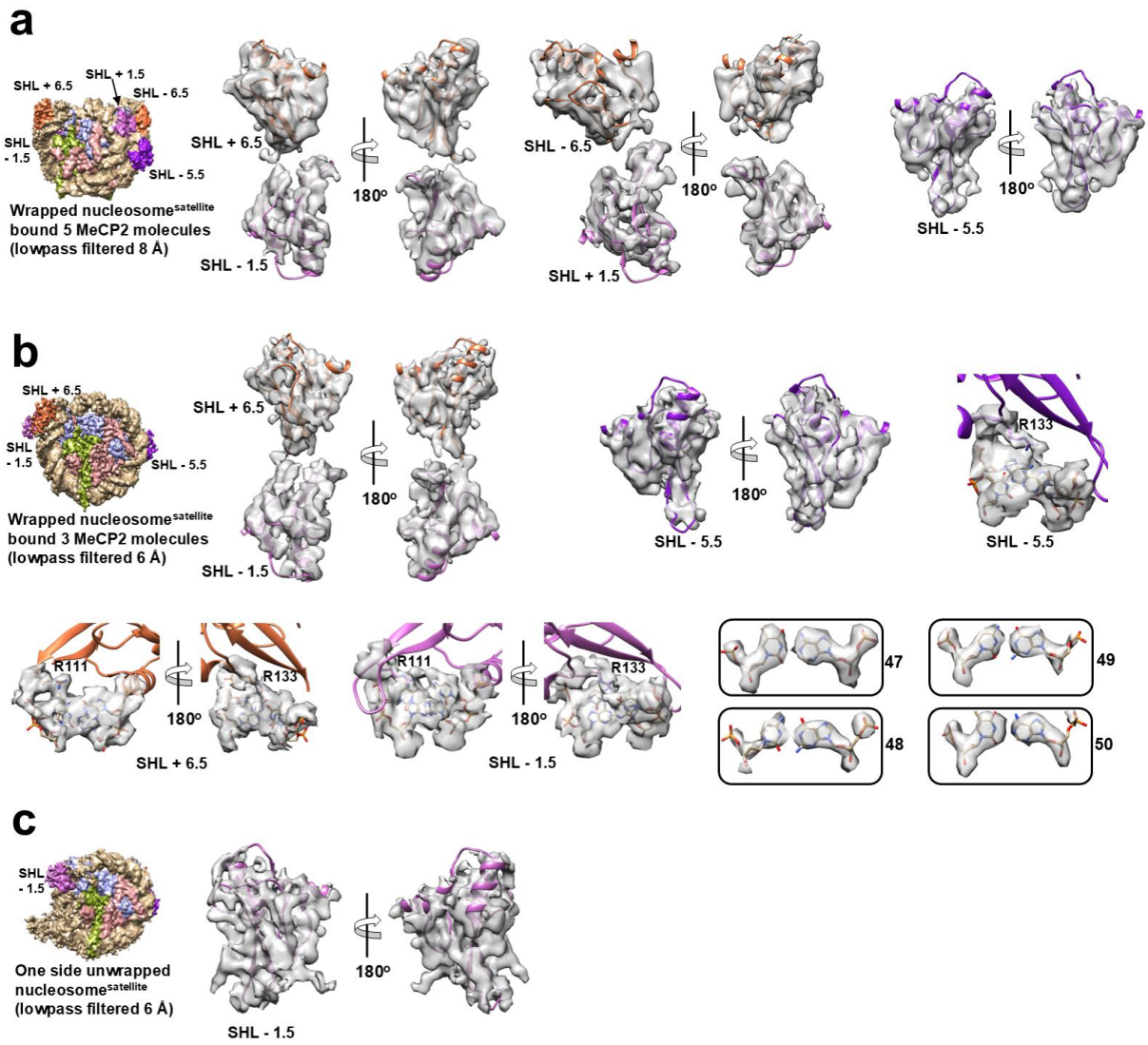
778

779 **Extended Data Fig. 3 | Cryo-EM data analysis of MeCP2-bound nucleosome601. a,**
780 Superposition of MeCP2 models into EM densities of nucleosome^{601} bound 2 MeCP2
781 molecules. **b,** Superposition of MeCP2 models into EM densities of nucleosome^{601} bound 1
782 MeCP2 molecule. **c,** Alignment of MeCP2-bound naked DNA (PDB: 6OGJ, palecyan) and
783 MeCP2-bound nucleosome^{601} (DNA: gray, MeCP2: orange, H3: blue). MeCP2 widens major
784 groove in naked DNA. Nucleosomal DNA major groove structure remains unchanged upon
785 MeCP2 binding.

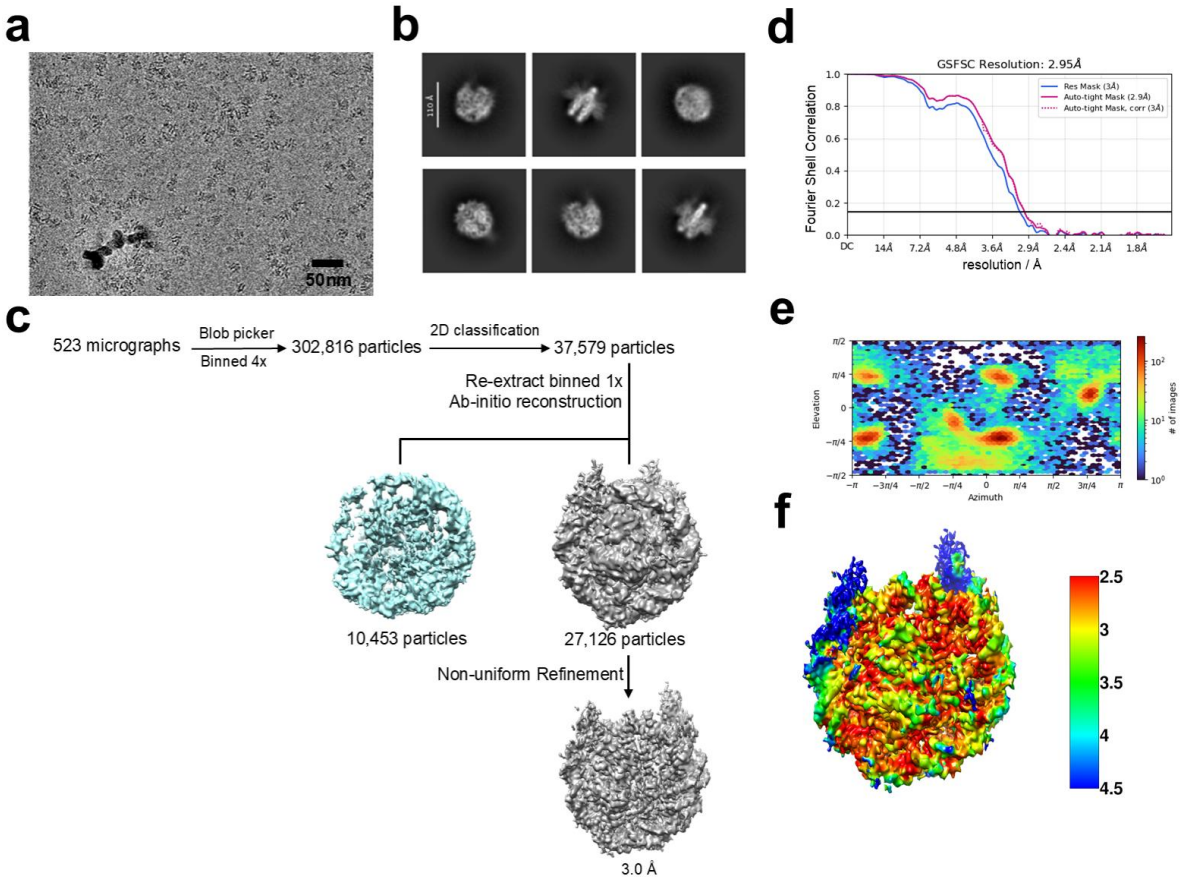
786



Extended Data Fig. 4 | Data processing for nucleosome^{satellite} engaged by MeCP2. a, Raw image. **b,** 2D classification results. **c,** Particle analysis. **d,** FSC curves. **e,** Particle orientation distribution. **f,** Local resolution.

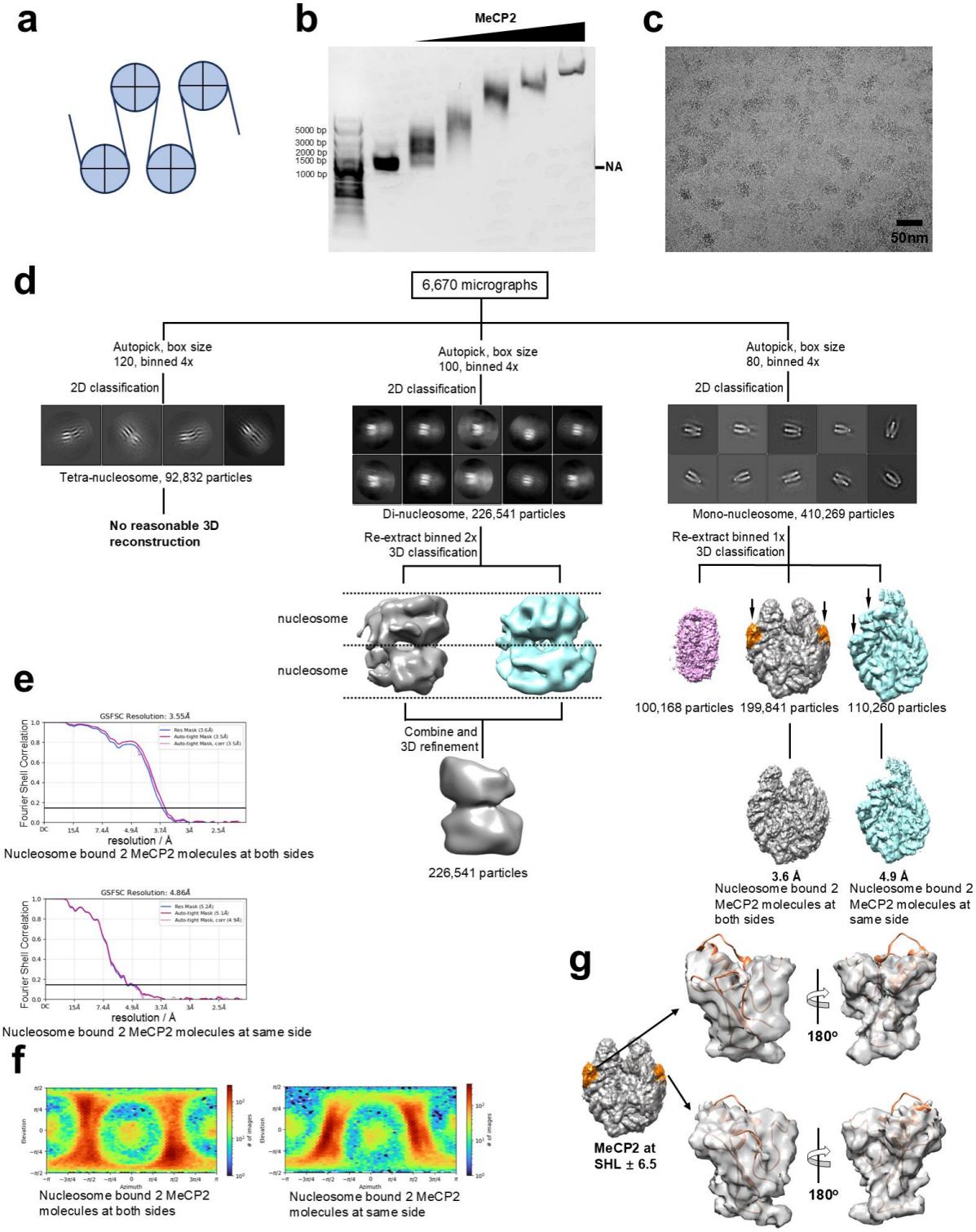


Extended Data Fig. 5 | Cryo-EM data analysis of MeCP2-bound nucleosome^{satellite}. a, Superposition of MeCP2 models into EM densities of nucleosome^{satellite} bound 5 MeCP2 molecules. The 5 MeCP2 molecule densities are located at SHL ± 6.5, SHL ±1.5, and SHL –5.5. EM map is lowpass filtered to 8 Å. **b,** Superposition of MeCP2 models into EM densities of nucleosome^{satellite} bound 3 MeCP2 molecules The 3 MeCP2 molecule densities are located at SHL + 6.5, SHL –1.5, and SHL – 5.5. EM map is lowpass filtered to 6 Å. The DNA density is good enough to build atomic model. Numbers of DNA base pairs in α-satellite DNA are shown at right side. **c,** Superposition of MeCP2 models into EM densities of one side unwrapped nucleosome^{satellite} bound MeCP2. EM map is lowpass filtered to 6 Å. Density of MeCP2 at SHL –1.5 is shown.

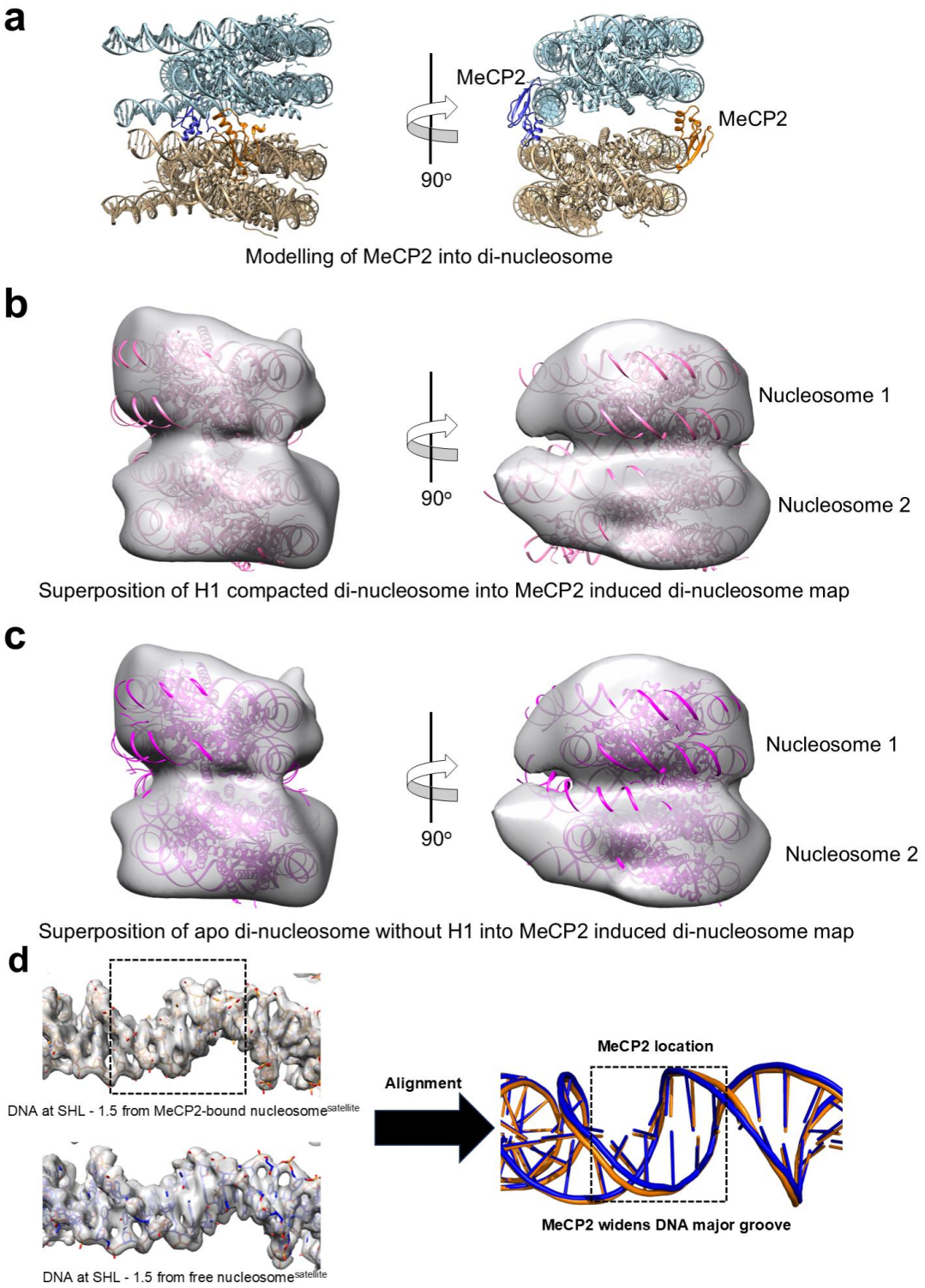


804

805 **Extended Data Fig. 6 | Data processing for free nucleosome^{satellite}. a,** Raw image. **b,** 2D
806 classification results. **c,** Particle analysis. **d,** FSC curves. **e,** Particle orientation distribution. **f,**
807 Local resolution.



Extended Data Fig. 7 | Data processing for NA bound MeCP2. a, Schematic diagram of NA. **b,** EMSA of the NA with MeCP2 titrated at molar ratios ([MeCP2]/[NA]) of 4:1, 8:1, 12:1, 16:1 and 20:1. **c,** Raw image. **d,** Particle analysis. **e,** FSC curves. **f,** Particle orientation distribution. **g,** Superposition of MeCP2 models into EM densities of mono-nucleosome bound 2 MeCP2 proteins at both entry/exit sides from NA bound MeCP2 data.



Extended Data Fig. 8 | Cryo-EM data analysis of MeCP2-bound NA. a, MeCP2 models are placed into the di-nucleosome from NA bound MeCP2 data. **b,** Superposition of di-nucleosome model from H1 compacted NA (PDB: 7PFC) into MeCP2 induced di-nucleosome map. **c,** Superposition of apo di-nucleosome model without H1 (PDB: 1ZBB) into MeCP2 induced di-nucleosome map. **d,** Alignment of DNA structures at SHL – 1.5 from MeCP2-bound nucleosome^{satellite} (orange) and free nucleosome^{satellite} (blue). MeCP2 location is indicated as dashed line rectangle. The left panel shows the superposition of DNA models into EM maps.

Table 1. Cryo-EM data collection and model refinement parameters

	Nucleosome^{601}-scFv-2 MeCP2 molecules PDB: 43GG EMDB ID: 81860	Nucleosome^{601}-scFv-1 MeCP2 EMDB ID: 81890	Nucleosome^{601}-scFv-2 MeCP2 molecules with extended ID EMDB ID: 81894	Nucleosome^{satellite}-scFv-5 MeCP2 molecules PDB: 43GQ EMDB ID: 81870	Nucleosome^{satellite}-scFv-3 MeCP2 molecules PDB: 43GR EMDB ID: 81871	Nucleosome^{satellite}-scFv-MeCP2 one side unwrap EMDB ID: 81876	Nucleosome^{satellite}-scFv-MeCP2 both sides unwrap EMDB ID: 81878
Data collection and processing							
Magnification	81,000	81,000	81,000	60,000	60,000	60,000	60,000
Voltage (kV)	300	300	300	300	300	300	300
Exposure time (s/frame)	0.08	0.08	0.08	0.08	0.08	0.08	0.08
Number of frames	50	50	50	50	50	50	50
Electron exposure (e–/Å^2)	50	50	50	50	50	50	50
Defocus range (μm)	-1.0 ~ -2.0	-1.0~ -2.0	-1.0 ~ -2.0	-1.0~ -2.0	-1.0 ~ -2.0	-1.0 ~ -2.0	-1.0 ~ -2.0
Pixel size (Å)	0.528	0.528	0.528	0.4015	0.4015	0.4015	0.4015
Symmetry imposed	C1	C1	C1	C1	C1	C1	C1
Initial particle images (no.)	2,198,708	2,198,708	2,198,708	1,763,152	1,763,152	1,763,152	1,763,152
Final particle images (no.)	326,121	318,663	153,877	31,945	38,615	93,735	46,018
Map resolution (Å)	2.8	3.0	3.9	2.9	2.8	2.8	2.8
FSC threshold	0.143	0.143	0.143	0.143	0.143	0.143	0.143
Map resolution range	2.4-7.2	2.4-7.4	3.5-10.2	2.4-8.9	2.3-8.4	2.4-10.1	2.4-10.2
Refinement							
Non-hydrogen atoms	17910			18400	17323		
Protein residues	1408			1606	1462		
Nucleotide	336			288	288		
Validation							
Bond lengths (Å)	0.005			0.010	0.010		
Bond angles (°)	1.003			1.215	1.23		
MolProbity score	1.9			2.4	2.46		
Clashscore	9.9			19.3	20.2		
Poor rotamers (%)	1.98			2.67	2.66		
Ramachandran Plot							
Favored (%)	97.10			95.47	95.17		
Allowed (%)	2.83			4.34	4.62		
Disallowed (%)	0.07			0.19	0.21		

834 **Table 1. Cryo-EM data collection and model refinement parameters (continued)**

	Free nucleosome^{satellite} EMDB ID: 81873	Di-nucleosome from NA EMDB ID: 81899	Nucleosome^{601}-2 MeCP2 molecules at two sides from NA EMDB ID: 81891	Nucleosome^{601}-2 MeCP2 molecules at same side from NA EMDB ID: 81898
Data collection and processing				
Magnification	60,000	81,000	81,000	60,000
Voltage (kV)	300	300	300	300
Exposure time (s/frame)	0.08	0.08	0.08	0.08
Number of frames	50	50	50	50
Electron exposure (e-/Å^2)	50	50	50	50
Defocus range (μm)	-1.0 ~ -2.0	-1.0~ -2.0	-1.0 ~ -2.0	-1.0~ -2.0
Pixel size (Å)	0.4015	0.528	0.528	0.528
Symmetry imposed	C1	C1	C1	C1
Initial particle images (no.)	302,816	729,642	729,642	729,642
Final particle images (no.)	27,126	226,541	199,841	110,260
Map resolution (Å)	3.0	25	3.6	4.9
FSC threshold	0.143	0.143	0.143	0.143
Map resolution range	2.4-6.2		3.2-10.9	4.2-12.5
Refinement				
Non-hydrogen atoms				
Protein residues				
Nucleotide				
Validation				
Bond lengths (Å)				
Bond angles (°)				
MolProbity score				
Clashscore				
Poor rotamers (%)				
Ramachandran Plot				
Favored (%)				
Allowed (%)				
Disallowed (%)				